Alma Mater Studiorum - Università di Bologna

School of Science

Department of Physics and Astronomy
Master Degree Programme in Astrophysics and Cosmology

Magnetic field in PSZ2G243.15-73.84 from MeerKAT polarisation observations

Graduation Thesis

Presented by:
Francesco Campolucci

Supervisor:
Chiar.ma Prof. Annalisa Bonafede

Co-supervisor:
Dr. C. Stuardi

Co-supervisor:
Dr. M. Balboni

Academic year 2024-2025
Graduation date 12/12/2025

Abstract

In this work, radio observations from MeerKAT and X-ray data from the CHEX-MATE survey of the galaxy cluster PSZ2G243.15-73.84 are combined with magnetic field simulations (performed with the MiRó code) to test the scaling relation between cluster mass and magnetic field, $B = B_{M'}(M/M')^b$ ($B - M$ relation) with $b = 1.33$, as found in Dolag et al. (2002) using cosmological simulations. The values tested for $B_{M'}$ and b are those derived in Balboni (2025b) by fitting a sample of galaxy clusters observed in both radio and X-rays, where two sets of best-fit parameters for the $B - M$ relation were obtained: in the first set, b was fixed at 1.33 while $B_{M'} = 2.11$ μG was determined from the fit; in the second set, both b and $B_{M'}$ were allowed to vary, yielding $b = 2.05$ and $B_{M'} = 2.52$ μG. A brief overview of the main topics relevant to this work is first provided, covering galaxy clusters, relaxed and disturbed systems, X-ray emission from the ICM and bremsstrahlung, radio emission in clusters, synchrotron radiation, polarisation of radiation, radio astronomy, interferometry, and the basics of calibration. The MeerKAT data were already calibrated prior to any further processing in this work. Nevertheless, a quality check is performed, leading to the decision to perform self-calibration to remove artifacts present in the initial image. After self-calibration, the artifacts either disappear or become much less significant, and the noise in the resulting image is closer to the theoretical value. The observed radiation is expected to be synchrotron emission, which is intrinsically highly linearly polarised. As the observed polarisation fraction is lower than the intrinsic one, several depolarisation effects must be present, including bandwidth depolarisation, beam depolarisation, and internal depolarisation. Bandwidth depolarisation is corrected by applying the rotation measure synthesis technique (RM-synthesis). As a result of the RM-synthesis, the linearly polarised intensity image (P) and the RM map are created. However, very few pixels exhibit significant polarised intensity in the resulting image-map, which leads to the decision to discard the RM map. The P image is used to extract the radial polarisation fraction profile, while excluding emission from the cluster's extended sources to avoid regions affected by internal depolarisation (radio halo) or in the foreground (relics). Consequently, the polarisation fraction profile is determined solely by beam depolarisation. A RM map is generated using the MiRó code, based on the magnetic field strength predicted by the $B - M$ relation under study. The code requires as input a magnetic field cube and a density cube. The magnetic field cube is generated by the code itself, assuming random phases, Gaussian components, and a power spectrum as described in Domínguez-Fernández (2019). The density cube is built from the density profile extracted from X-ray observations taken with the XMM-Newton telescope for the CHEX-MATE project. In addition, this work incorporates scatter for the density profile, something that had not been accounted for in previous studies of this kind. Finally, the simulated RM map is generated and used to produce a simulated polarisation fraction profile, accounting for beam depolarisation, which is the dominant source of depolarisation in the observed profile. The comparison between the observed and simulated profiles does not result in a match, leading to the conclusion that this cluster does not follow the $B - M$ relation.

The thesis is organized as follows: in Chapter1, a brief recap of topics relevant to this work is presented; in Chapter 2, the workflow and methodology employed to achieve the intended objectives are described, together with a presentation of the data and the instruments used to obtain them; in Chapter 3, the first produced total intensity I image from the radio data is shown and discussed; in Chapter 4 the self-calibration

procedure used to improve the image quality is presented; in Chapter 5 the the post self-calibration images produced in total intensity I and in polarised intensity (Stokes Q and U) are shown; in Chapter 6 the implementation of RM-synthesis to correct for bandwidth depolarisation is presented; in Chapter 7 the extraction of the density profile needed for the MiRó code from X-ray observations is reported; In Chapter 8 the derivation of the observed and simulated polarisation fraction profiles, respectively from the RM-synthesis corrected radio images and from the MiRó code, is described, along with their comparison; In Chapter 9 a summary of the work and the final conclusions are provided.

Contents

Chapter 1

Background Theory

1.1 Galaxy clusters

Galaxy clusters are the largest virialized systems in the universe, typically with a virial radius of 1.5-3 Mpc. They are made of DM, galaxies and gas, for a total mass of $M = 10^{13} - 10^{15} M_{\odot}$. Around 83% of the mass is in the DM component, the remaining 17% is baryonic, of which 15% is gas and 2% is galaxies. Galaxy clusters can contain thousands of galaxies, moving with a velocity dispersion of $\sigma_v \sim 1000$ km/s, with early-type galaxies (ETGs) forming the dominant population. Because galaxies are both numerous and fast-moving, clusters become environments where close encounters are frequent, and these interactions influence their evolution. Even if there are many galaxies, the main baryon component is the fully ionized gas that fills the whole cluster, the ICM (Intra-Cluster Medium). The ICM forms a halo of hot gas that is in hydrostatic equilibrium within the cluster's gravitational potential well. The ICM is characterized by high temperature $T = 10^7 – 10^8\ K$, low density $n = 10^{-3} – 10^{-4}$ cm^{-3} and sub solar metallicity $Z = 0.3 Z_{\odot}$. Galaxies not only interact between themselves, but also maintain ongoing interactions with the ICM, which influence their morphology.

1.2 ICM X-ray emission and bremsstrahlung

X-ray emission from the ICM is dominated by bremsstrahlung, recombination, and emission lines.

Bremsstrahlung originates from Coulomb collisions between electrons and ions in a plasma, during which the electrons are accelerated and consequently lose energy by emitting radiation. The energy lost by an electron in a single collision can be described using the Larmor formula

$$-\left(\frac{d\varepsilon}{dt}\right)_{br} = \frac{2}{3}\frac{e^2}{c^3}a^2 = \frac{2}{3}\frac{e^2}{c^3}\left(\frac{-Ze^2}{m_e r}\right)^2, \tag{1.2.1}$$

where ϵ is the energy of the electron, t is the time, a is the acceleration due to Coulomb force, e is the charge of the electron, c is the speed of light, m_e is the mass of the electron, r is the distance between the electron and the ion and Z is the charge of the ion. For a population of electrons and ions in thermal equilibrium, following the Maxwell-Boltzmann velocity distribution, the emissivity of the electrons is given by

$$j_{br}(\nu, T) = 6 \cdot 10^{-38} g_{ff}\,(\nu, T, Z)\, n_e n_i Z^2 T^{-1/2} e^{-h\nu/kT}\ [\mathrm{erg} \cdot \mathrm{s}^{-1} \cdot \mathrm{cm}^{-3} \cdot \mathrm{Hz}^{-1}], \tag{1.2.2}$$

where ν is the frequency, k is the Boltzmann constant, n_i is the ion number density, T is the temperature and g_{ff} is the Gaunt Factor. For the typical densities and temperatures of the ICM, bremsstrahlung emission reaches the X-ray band. The bolometric emissivity is obtained integrating over the frequency

$$j_{br}(T) = 2.4 \cdot 10^{-27} \overline{g}_{ff}\,(T, Z)\, n_e n_i Z^2 T^{1/2}\ [\mathrm{erg} \cdot \mathrm{s}^{-1} \cdot \mathrm{cm}^{-3}], \tag{1.2.3}$$

where $\overline{g}_{ff}$ is the average Gaunt Factor. The cooling time, which is the time it takes for the gas to radiate all its energy through bremsstrahlung, is

$$t_{br} = \frac{E}{|dE/dt|} = \frac{3/2(n_e + n_i)kT}{j_{br}(T)} = \frac{6 \cdot 10^3}{n_e Z^2 \overline{g}_{ff}} T^{1/2}\ [\mathrm{yr}], \tag{1.2.4}$$

where E is the total amount of gas thermal energy and $|dE/dt|$ is the energy loss by bremsstrahlung (Eq.1.2.3). Considering the density and temperature of the ICM, the cooling time exceeds 10 Gyr. Moreover, bremsstrahlung is the dominant cooling process at temperatures above $T = 10^7$ K, implying that all galaxy clusters emit bremsstrahlung radiation and are therefore X-ray sources. The surface brightness of bremsstrahlung is given by

$$I_{br}(\nu) = \frac{j_{br}(\nu, T)}{\alpha_{br}(\nu, T)} \left(1 - e^{-\tau_\nu}\right) = \begin{cases} h\nu/kT << 1;\ \tau_\nu >> 1 \text{ opt. thick: } \propto \nu^2 \\ h\nu/kT << 1;\ \tau_\nu << 1 \text{ opt. thin: const} \\ h\nu/kT >> 1;\ \tau_\nu << 1 \text{ opt. thin: } \propto e^{-h\nu/kT} \end{cases}, \tag{1.2.5}$$

where α_{br} is the absorption coefficient for bremsstrahlung and τ_ν is the optical depth. Hence, the bremsstrahlung spectrum is approximately constant as a function of frequency up to the exponential cut-off. For the typical density and temperature of the ICM, the bremsstrahlung emission has an energy cutoff in the X-ray band. At low frequencies, bremsstrahlung is self-absorbed as photons are absorbed by free electrons in the presence of the Coulomb field of ions, producing a spectral dependence $\propto \nu^2$. However, this process does not occur in the X-ray band for galaxy clusters.

Bremsstrahlung photons are polarised with the electric field vector perpendicular to the plane of interaction. However, because these planes are randomly oriented due to the electrons' random motion in the plasma, the net polarisation averages to zero.

In addition to bremsstrahlung, the X-ray spectrum of the ICM includes emission lines from highly ionized heavy elements, such as the Fe-L complex and the Fe-Kα lines. Line emission becomes increasingly important at lower ICM temperatures, but bremsstrahlung remains the dominant emission process. Both line emission and Bremsstrahlung are associated to two body processes, so their emissivity is proportional to n_e and n_i, so that the total emissivity can be written as

$$j_{tot,\nu} = n^2 \Lambda(T, Z) \tag{1.2.6}$$

where n is the density, Z is the metallicity and Λ is the cooling function. The emissivity depends more on the density than on the cooling function (hence on the temperature).

A detailed discussion of bremsstrahlung and line emission can be found in Rybicki and Lightman (2004).

1.3 Relaxed and disturbed clusters

Galaxy clusters can be divided into two groups: relaxed and disturbed.

Radial profiles of the ICM reveal differences between relaxed and disturbed clusters. Sanderson et al. (2009) and Hudson (2010) showed that relaxed clusters possess dense, cuspy cores, while disturbed clusters have flatter core density profiles. In the innermost regions, the gas density in relaxed clusters is higher than in disturbed systems, but this contrast decreases with radius. Entropy profiles are also different for the two kind of clusters: relaxed clusters have rising entropy with radius, whereas disturbed clusters show flatter entropy distributions. For temperature profiles: relaxed clusters have a central temperature drop, while disturbed clusters have relatively flat or slightly rising temperature profiles in their cores.

In relaxed clusters, the ICM in the central regions has high density and low temperature, leading to a short cooling time. The gas cools and loses support creating a cooling flow. This flow supplies cold gas for star formation in the brightest cluster galaxy (BCG). Observationally, BCGs in relaxed clusters have elevated star formation rates, consistent with being fed by the cooling flow (Sanderson et al., 2009). Alternatively, the falling gas fuels accretion onto the central supermassive black hole.

In Rasia (2013), X-ray morphology is used to distinguish between relaxed and disturbed galaxy clusters. Relaxed clusters typically show peaked and centrally concentrated X-ray emission, with symmetric and regular surface brightness distributions, indicating a dynamically stable state. Disturbed clusters have flatter and less concentrated emission, significant asymmetries, and substructures such as multiple brightness peaks, which reflect ongoing mergers or dynamical activity.

Both types of clusters are associated with different kinds of extended structures producing non-thermal radio emission (synchrotron): radio halos, radio mini-halos and relics. Halos and relics are typically associated with disturbed clusters, whereas mini-halos are associated with relaxed clusters. This is discussed in the next section.

1.4 Radio emission in clusters

The information reported in this section and more can be found in van Weeren (2019), Feretti (2012) and Bonafede (2010b).

Three types of diffuse radio sources emitting synchrotron radiation are observed in galaxy clusters: radio halos, radio mini-halos, and radio relics.

Radio halos are in the center of galaxy clusters, typically extending over scales of $\gtrsim 1$ Mpc. They are not associated with any individual radio galaxy and have no optical counterpart. Their morphology is generally regular and diffuse, with very low surface brightness on the order of $\sim 1\ \mu\text{Jy/arcsec}^2$ at 1.4 GHz. Radio halos exhibit a steep spectral index, $\alpha \sim 1 - 2$, and are typically unpolarised. They are most commonly found in merging or dynamically disturbed clusters.

Radio mini-halos share many properties with giant radio halos, such as low surface brightness, regular morphology, and lack of an optical counterpart. However, they are smaller in size, typically a few $100 - 500$ kpc. Their spectral index is steep, $\alpha \sim 1 - 1.3$, but slightly flatter than that of giant halos. They are generally unpolarised, but still with higher polarisation fraction than giant halos. Unlike giant halos, mini-halos are predominantly found in relaxed, non merging clusters.

Radio relics are typically found in the cluster outskirts and exhibit arc like structures oriented roughly perpendicular to the cluster radius. Like halos, they are not associated with any radio galaxy, have no optical counterpart and present low surface brightness. Relics can extend over scales of $\gtrsim 1$ Mpc and generally have a steep spectral index,

$\alpha \sim 1-1.3$. Unlike radio halos and mini-halos, they are strongly polarised (20-30% at 1.4 GHz), with magnetic fields aligned along their major axis. They are most commonly observed in merging or dynamically disturbed clusters.

1.5 Synchrotron radiation

Synchrotron radiation is produced by relativistic electrons spiraling around magnetic fields. Electrons are accelerated by the Lorentz force $\vec{F}_L = -e(\vec{v}\times\vec{B})$, and consequently radiate energy. The energy lost by an electron can be expressed using the relativistic Larmor formula

$$-\left(\frac{d\varepsilon}{dt}\right)_{sy} = \frac{2}{3}\frac{e^2}{c^3}\gamma^2 a^2 = \frac{c}{6\pi}\sigma_T \beta^2\gamma^2 B^2, \tag{1.5.1}$$

where γ is the Lorentz factor, $\beta = v/c$ with v being the speed of the electron, a is the acceleration due to Lorentz force, σ_T is the Thomson cross-section and B is the magnetic field strength. Considering a population of relativistic electrons with energy distribution

$$N(E) = N_0 E^{-\delta}, \tag{1.5.2}$$

where N_0 is the normalization and δ is the slope, the synchrotron emissivity becomes

$$j_{sy}(\nu) = \frac{e^3 \mathrm{N}_0 B}{\sqrt{3}\pi m_e c^2(\delta+1)}\Gamma\left(\frac{\delta}{4}+\frac{19}{12}\right)\Gamma\left(\frac{\delta}{4}-\frac{1}{12}\right)\left(\frac{m_e c\nu}{2eB}\right)^{-\frac{\delta-1}{2}} = C(\delta)N_0 B^{\frac{\delta+1}{2}}\nu^{-\frac{\delta-1}{2}}, \tag{1.5.3}$$

where $C(\delta)$ collects all the constants and Γ is the gamma function. The spectral index (slope of the synchrotron emission) is $\alpha = (\delta-1)/2$, therefore

$$j_{sy}(\nu) = C(\alpha)N_0 B^{\alpha+1}\nu^{-\alpha}. \tag{1.5.4}$$

The surface brightness of synchrotron emission is given by

$$I_{sy}(\nu) = \frac{j_{sy}(\nu,T)}{\alpha_{sy}(\nu,T)}\left(1-e^{-\tau_\nu}\right) = \begin{cases} \tau_\nu >> 1 \text{ opt. thick: } \propto B^{-1/2}\nu^{5/2} \\ \tau_\nu << 1 \text{ opt. thin: } \propto B^{\alpha+1}\nu^{-\alpha} \end{cases}, \tag{1.5.5}$$

where α_{sy} is the absorption coefficient for synchrotron. The radiation is linearly polarised with the electric field vector perpendicular to the projection of the magnetic field onto the plane of the sky. For a power law distribution of emitting electrons, the maximum (magnetic field is never completely ordered) polarisation fraction in the optically thin regime is $f_{pol} = (3\delta+3)/(3\delta+7)$, while in the optically thick regime it becomes $f_{pol} = 3/(16\delta+13)$. For example, when $\delta = 3$ (equivalently $\alpha = 1$), the maximum polarisation fraction reaches 75%. Since synchrotron emission is linearly polarised, the circular polarisation component, Stokes V, is zero.

A detailed discussion of synchrotron emission can be found in Rybicki and Lightman (2004).

1.6 Polarisation and Stokes parameters

Depending on the orientation of the electric field E (or magnetic field) radiation may be linearly, circularly (right or left), or elliptically polarised (right or left). If E oscillates always in the same plane, the polarisation is linear. If it rotates around the propagation

axis of the wave, tracing a circle, the polarisation is circular. If it traces an ellipse, the polarisation is elliptical. If a wave is unpolarised, E does not have a preferred orientation, but has a random orientation over time.
Considering an electromagnetic wave propagating in the z direction (assume $z = 0$), the two components of the electric field are

$$E_x(t) = E_{x,0}(t)cos(\omega t + \delta_x(t)) \ , \ E_y(t) = E_{y,0}(t)cos(\omega t + \delta_y(t)), \tag{1.6.1}$$

where E_0 is the amplitude of the electric field, ω is the angular frequency and δ is the phase. The polarisation ellipse (valid at each t), described by the cartesian components of E vectors of electromagnetic, is found by removing the ωt term

$$\left(\frac{E_x(t)}{E_{x,0}(t)}\right)^2 + \left(\frac{E_y(t)}{E_{y,0}(t)}\right)^2 - 2\frac{E_x(t)E_y(t)}{E_{x,0}(t)E_{y,0}(t)}\cos\delta(t) = \sin^2\delta(t), \ \delta = \delta_y - \delta_x. \tag{1.6.2}$$

Its orientation determines the polarisation properties of the wave. Considering monochromatic waves and averaging over time

$$\left(E_{x,0}^2 + E_{y,0}^2\right)^2 = \left(E_{x,0}^2 - E_{y,0}^2\right)^2 + \left(2E_{x,0}E_{y,0}\cos\delta\right)^2 + \left(2E_{x,0}E_{y,0}\sin\delta\right)^2. \tag{1.6.3}$$

The Stoke parameters (Stokes, 1851) are defined as

$$I = E_{x,0}^2 + E_{y,0}^2 \ , \ Q = E_{x,0}^2 - E_{y,0}^2 \ , \ U = 2E_{x,0}E_{y,0}\cos\delta \ , \ V = 2E_{x,0}E_{y,0}\sin\delta. \tag{1.6.4}$$

Hence, the equation of the polarisation ellipse of totally polarised light is

$$I^2 = Q^2 + U^2 + V^2, \tag{1.6.5}$$

instead, for partial polarisation

$$I^2 > Q^2 + U^2 + V^2. \tag{1.6.6}$$

The Stokes parameters are intensities (which are measurable quantities), I is total intensity, $\sqrt{Q^2 + U^2 + V^2}$ is the total polarised intensity, V is the circular polarised intensity and $\sqrt{Q^2 + U^2}$ is the linear polarised intensity, having polarisation angle

$$\psi = \frac{1}{2}\arctan\left(\frac{U}{Q}\right). \tag{1.6.7}$$

1.7 Basics of radioastronomy

This section is based on the content presented in Condon and Ransom (2016).

Radio photons ($\nu = 10$ MHz $- 1$ THz) are not energetic enough to induce the photoelectric effect. Therefore, in the radio band the wave formalism is used to describe the incoming signal, which is valid due to the high number of photons. An antenna collects the incoming electromagnetic radiation and converts it into a voltage, thanks to the electric field $\vec{E}$ carried by the signal, making the electrons in the receiver oscillate. The angular distribution of the power received by the antenna is called beam. The beam of a uniformly illuminated circular aperture is known as the Airy pattern. It presents a central main peak surrounded by concentric secondary peaks separated by zeros. The central peak of the beam is called the main beam, which is the region containing the principal response. The smaller surrounding peaks are named sidelobes. The angular resolution is defined through the half-power beamwidth ($HPBW$)

$$\theta_{res} \approx \frac{\lambda}{D}, \tag{1.7.1}$$

where D is the aperture size of the antenna and λ is wavelength of the observation. The instrument is diffraction limited in the best possible scenario. The beam width between the first nulls (BWFN) defines the field of view (FoV), that is, the observable portion of the sky

$$\theta_{FoV} = \frac{2\lambda}{D}. \tag{1.7.2}$$

For single-dish radio telescopes, the angular resolution and field of view are comparable, which limits their imaging capabilities. Improving the resolution by observing at higher frequencies is constrained by the boundaries of the radio band (atmospheric absorption). Alternatively, increasing the antenna diameter is limited by practical constraints on the physical size of the instrument.

The solution is interferometry, an array of N antennas working together. Each pair of dishes is described by its baseline b, namely the distance between them. Each pair is sensitive to a single angular scale

$$\theta = \frac{\lambda}{b}. \tag{1.7.3}$$

To be precise, the denominator is the projected baseline as seen from the source, $b \sin\theta$, with θ being the angle between the baseline and the line of sight (L.o.S.). The FoV remains the same as that of the single antennas comprising the interferometer. However, the angular resolution is improved, and in Eq.1.7.1, the aperture is replaced by the maximum distance between the antennas

$$\theta_{res} = \frac{\lambda}{b_{max}}, \tag{1.7.4}$$

where b_{max} is the longest baseline. Contrary to single dishes, which have a maximum angular resolution but no minimum one, an interferometer also has a minimum angular scale, determined by its shortest baseline b_{min}. There is a lower limit to b_{min}, since two antennas cannot be superimposed and must be separated by at least the sum of their dish radii. This is problematic, as the total flux of resolved sources cannot be fully recovered

$$\theta = \frac{\lambda}{b_{min}}. \tag{1.7.5}$$

Thus, interferometers are sensitive only to an angular range $\lambda/b_{max} < \theta < \lambda/b_{min}$. Another difference from single dishes is that, with interferometry, imaging becomes possible because the field of view remains that of the individual antennas, making it much larger than the angular resolution.

The most basic interferometer consists of two antennas. The signal from the source reaches the pair, and each antenna generates a voltage that is subsequently correlated with that of the other. The antenna pair has its own beam: a cosine multiplied by the beam of the individual antennas. The point source response of the interferometer is known as the dirty beam. Improving the point-source response of an interferometer requires more baselines and therefore more antenna pairs. Short baselines are sensitive to extended sources, while long baselines are sensitive to compact sources. Using the superposition principle, the beam of the interferometer can also be generalized to extended sources (over the sky Ω) with brightness $I'(\hat{s})$. The response is called complex visibility V:

$$V = \int I'(\hat{s}) e^{-i2\pi \overrightarrow{b} \cdot \hat{s}/\lambda} d\Omega. \tag{1.7.6}$$

The complex visibility and the sky brightness are a Fourier pair, meaning that one is obtained from the other through a Fourier transform. The forward Fourier transform (FT) is defined as

$$F(s) = \int_{-\infty}^{\infty} f(x) e^{-2\pi isx} dx \tag{1.7.7}$$

and the inverse transform (FT^{-1}) as

$$f(x) = \int_{-\infty}^{\infty} F(s) e^{2\pi isx} ds. \tag{1.7.8}$$

where x and s are generic variables associated with the functions f and F. Extending to three dimensional space, the response is expressed over the uv plane, a plane perpendicular to the source direction, where u and v are related to l and m, the direction cosines defining the position on the sky. A third coordinate, w, accompanies u and v, but under the flat sky approximation it is reduced to be $w = 0$. The coverage of this plane is determined by the distribution of baselines, measured in units of λ, as seen from the source. A single baseline samples one point in the plane, so computes the FT of the brightness. Observations sample the visibility function (sampled visibility), and by applying an inverse Fourier transform, FT^{-1}, the sky brightness distribution can be reconstructed to generate an image

$$I'(l,m) = \iint V(u,v) e^{2\pi i(ul+vm)} dudv. \tag{1.7.9}$$

On the other hand, the visibility function can be obtained by Fourier transforming the sky brightness

$$V(u,v) = \iint I'(l,m) e^{-2\pi i(ul+vm)} dldm. \tag{1.7.10}$$

1.8 Calibration

Calibration involves measuring the effect of several corruptions, known as complex gains G_{ij}, on observed visibilities, to derive corrections to apply onto observations of the target.

$$V_{ij}^{obs}(\nu,t) = G_{ij}(\nu,t) V_{ij}^{true}(\nu,t), \tag{1.8.1}$$

where V_{ij}^{true} is the true visibility without corruptions, V_{ij}^{obs} is the visibility observed and i & j denote baseline antennas. G_{ij} can be approximated as the product of the two associated antenna-based complex gains: $G_{ij} = G_i G_j^*$. Both visibility and gain are complex numbers characterized by amplitude and phase:

$$V_{ij} = A_{ij} e^{i\phi_{ij}}, \quad G_i = a_i e^{i\theta_i}, \quad G_j^* = a_j e^{-i\theta_j}. \tag{1.8.2}$$

Where A_{ij} and ϕ_{ij} are the baseline-related amplitude and phase respectfully, and $a_{i,j}$ and $\theta_{i,j}$ are the antenna-related corrections for amplitude and phase. Substituting equations Eq.1.8.2 into equation Eq.1.8.1 gives:

$$A_{ij}^{obs} e^{i\phi_{ij}^{obs}} = A_{ij}^{true} a_i a_j e^{i(\phi_{ij}^{true} + \theta_i - \theta_j)}. \tag{1.8.3}$$

To obtain the unknown quantity A_{ij}^{true}, a model can be introduced for which the true amplitude (A_{ij}^{model}) and phase (θ_{ij}^{model}) are known. Considering a bright point source observed at the phase center:

$$A_{ij}^{model} = \text{constant flux S}, \quad \phi_{ij}^{model} = 0. \tag{1.8.4}$$

In practice, the gains G_{ij} are determined by observing calibrator sources. For a calibrator observed at the phase center, the measured amplitude and phase relate to the model as

$$\begin{aligned} A_{ij}^{\text{obs}} &= G_i G_j^* \, A_{ij}^{\text{mod}} \quad \longrightarrow \quad A_{ij}^{\text{mod}} = \frac{A_{ij}^{\text{obs}}}{G_i G_j^*}, \\ \phi_{ij}^{\text{obs}} &= \theta_i - \theta_j + \phi_{ij}^{\text{mod}} \quad \longrightarrow \quad \phi_{ij}^{\text{mod}} = -\theta_i + \theta_j + \phi_{ij}^{\text{obs}}. \end{aligned} \tag{1.8.5}$$

More than one calibrator is generally required to satisfy the conditions for a reliable model. A primary calibrator, usually a bright non-variable QSO of known flux, is observed at the beginning of the observation for enough time to reach high S/N (signal to noise ratio), setting the absolute amplitude scale. A secondary calibrator, also a point-like QSO, is regularly observed before and after the target and must be located close to it (<3-5 degrees), to track time-dependent gain variations. The derived gains are then interpolated in time and applied to the target data, ensuring accurate calibration for imaging.

For a detailed discussion of calibration see Taylor et al. (1999).

Chapter 2

This thesis

2.1 Aim and workflow

The focus of this work is the galaxy cluster PSZ2G243.15-73.84. The goal is to infer the properties of its magnetic field and to determine if it follows the mass-magnetic field relation discovered in Dolag et al. (2002) and further analyzed by Balboni (2025b). The former showed, using cosmological simulations, that the temperature of the cluster and its magnetic field are linked in the following way

$$\langle B \rangle = A\, T^{\alpha} \tag{2.1.1}$$

where $\langle B \rangle$ is the mean magnetic field of the cluster inside its virial radius and T is the mass-weighted temperature inside r_{vir}. For an initial magnetic field seed of 10^{-9} [G] in the ΛCDM model, the exponent α is equal to 2. Therefore, for a virialized cluster

$$B \propto M^{(2/3)\alpha} \propto M^{1.33} \tag{2.1.2}$$

In Balboni (2025b) this relation is further analyzed by studying a sample of 16 CHEX-MATE-LoTSS clusters at redshift z $<$ 0.4. The previous proportionality can be expressed in a normalized form as $B = B_{M'}(M/M')^{b}$ ($B - M$ relation), where $B_{M'}$ is the mean magnetic field of the sample and $M' = 5.3 \cdot 10^{14} M_{\odot}$ is the median mass of the sample. Fitting this relation to the data while fixing $b = 1.33$ as found in Dolag et al. (2002) yields $B_{M'} = 2.11 \pm 0.88$ μG. Instead, allowing b to vary freely, the best fit values are $B_{M'} = 2.52 \pm 0.61$ μG and $b = 2.05 \pm 0.36$. The $B - M$ relation predicts a magnetic field for PSZ2G243.15-73.84 of 3.7 μG for the first fit and 6.0 μG for the second fit. This cluster is particularly interesting due to its higher redshift, $z = 0.41$, extending beyond the range studied in Balboni (2025b). Therefore, it provides an initial test of the validity of the mass-magnetic ($B - M$) field relation at larger distances.

To verify whether the predicted values match the true magnetic field strength of the cluster, PSZ2G243.15−73.84 was observed in the radio band with the MeerKAT telescope (details of the observation are provided in Sec.2.5).The objective is to extract a polarisation fraction profile and a RM map from the radio data. These observed maps are then compared with simulated counterparts generated using the MiRó code (Sec.8.1), where the simulations assume the magnetic field strength predicted by the $B - M$ relation. This comparison allows to assess whether the strength of the magnetic field corresponds to the prediction of the $B - M$ relation.

Although the observational data of the cluster were already calibrated when received for this work, a quality check is performed by producing the total intensity (I) image to ensure the data meet the required standards and to assess whether further calibration is necessary. Once this check and any necessary calibrations are complete, the analysis can begin. In the radio band, the expected continuum emission is synchrotron radiation originating from the cluster as well as from discrete sources along the line of sight, which may lie in the foreground or background of the cluster. Synchrotron radiation has an intrinsically high degree of linear polarisation. However, the emission from sources within or behind the cluster is affected by Faraday rotation as it propagates through an ionized, magnetized medium. Hence, bandwidth depolarisation and beam depolarisation decrease the level of linear polarisation of the synchrotron emission. In addition, for extended synchrotron emitting sources (the radio halo), within the cluster, internal depolarisation is also present. RM-synthesis (RM as rotation measure) can be used to correct for bandwidth depolarisation and to produce both a RM map and a linearly polarised intensity (P) image. Consequently, the polarisation fraction can be obtained by computing P/I. The polarisation fraction image and RM map can be used to extract the radial polarisation fraction profile and the radial RM profile. It is important to note that the extended emission within the cluster also undergoes internal depolarisation. For this reason, the radio halo is excluded when extracting the profiles. The relics must also be excluded, since they are foreground sources. In this way, the depolarisation affecting the polarisation fraction profile is due only to beam depolarisation. Once the observed polarisation fraction profile and RM map are obtained, the simulated counterparts must also be produced to make a comparison and verify the validity of the $B - M$ relation. The MiRó code is used to generate the simulated RM map, taking as input the predicted mean magnetic field within R_{500}, as given by the $B - M$ relation. The simulated RM map is then used to estimate the amount of beam depolarisation, from which a simulated polarisation fraction profile is constructed. Finally, the observed and simulated RM maps and polarisation fraction profiles are compared to determine whether the $B - M$ relation holds or not. A good agreement would support the relation, whereas a significant discrepancy would indicate that it does not apply to this cluster.

In summary, the analysis proceeds through the following steps:

1. Check for the quality of the radio data by looking at the total intensity image.
2. If needed, perform further calibration.
3. Produce images needed for the RM-synthesis.
4. Perform the RM-synthesis to correct for bandwidth depolarisation.
5. Obtain the linear polarised intensity (P) image and RM map.
6. Extract the polarisation fraction radial profile and the RM radial profile.
7. Extract the density profile from X-ray observations.
8. Generate the density cube.
9. Use the MiRó code to simulate the magnetic field of the cluster and create a magnetic field cube.
10. Use the MiRó code to compute a simulated RM map.

11. Create a simulated polarisation fraction profile introducing the effect of beam depolarisation.

12. Compare the observed and simulated polarisation fraction profiles and RM maps to test the validity of the $B-M$ relation.

2.2 MeerKAT

The MeerKAT[1] telescope is a radio interferometer located 90 km outside the small Northern Cape town of Carnarvon, in the semiarid Karoo region. The array consists of 64 antennas, each with a steerable main reflector (dish) of 13.5 m diameter and a secondary reflector of 3.8 m diameter. The configuration of the array is variable and selected according to the scientific goals of each observation. The majority of the antennas, 48, are concentrated in a central area of about half km in radius, while the longest baseline is 8 km. The main reflector consists of 40 aluminium panels, and together with the secondary reflector, the combined surface accuracy is maintained within 0.6 mm RMS (root mean square) of the ideal shape. The antenna employs an 'Offset Gregorian' optical design, in which no struts obstruct the incoming radiation. This configuration provides high sensitivity and excellent imaging quality. The antenna is equipped with three receivers: L band (900-1.670 MHz), UHF (580-1.015 MHz), and S band (1.75-3.5 GHz). The antenna structure allows observations over an elevation range of 15° to 88° and an azimuth range from -185° to +275°, with north defined as 0°. The main reflector can be pointed with high precision, achieving an accuracy of up to 5 arcseconds.

2.3 XMM-newton

XMM-Newton[2] is a 10.8 meters long, ∼4000 kg satellite. It boards three X-ray telescopes, each with 58 nested Wolter I grazing-incidence gold-coated mirrors in coaxial and cofocal configuration. The focal length is 7.5 meters, and the largest mirror has a diameter of 70 cm. The on-axis PSF (point spread function) ranges from $5''$ to $15''$, depending on the photon energy and whether FWHM (full width at half maximum) or HEW (half energy width) is considered. The mirrors are nested to maximize the collecting area, providing optimal effective area across 0.1-10 keV (around 1000 cm^2). The satellite carries three instruments: the European photon imaging cameras (EPIC), two reflection grating spectrometers (RGS), and an optical monitor (OM). The EPIC system consists of two MOS-CCD cameras and one pn-CCD: the MOS cameras are optimized for detecting low-energy X-rays, while the pn-CCD is designed to capture higher-energy X-rays. The RGS instruments specialize in high-resolution spectroscopy. The optical monitor (OM) is a Ritchey-Chrétien telescope providing simultaneous ultraviolet and optical observations.

---

[1] MeerKAT telescope overview: `https://www.sarao.ac.za/science/meerkat/about-meerkat/`

[2] Overview of XMM-Newton telescope: `https://www.cosmos.esa.int/web/xmm-newton/about-xmm-newton/`

2.4 CHEX-MATE

CHEX-MATE stands for Cluster HEritage project with XMM-Newton - Mass Assembly and Thermodynamics at the Endpoint of structure formation (Arnaud, 2020). This project focuses on observing in X-ray a sample of 118 local clusters detected by Planck via their Sunyaev-Zel'dovich effect, with the following goals:

1. Obtain the statistical properties for the local cluster population.
2. Deepen the understanding about non-gravitational heating.
3. Improve mass estimations.
4. Uncover how baryon collapse in the dark matter halo and cluster mergers affect the gas.

2.5 PSZ2G243.15-73.84

Information about this cluster is collected in Balboni (2025a). PSZ2G243.15-73.84 is a disturbed galaxy cluster located at z = 0.41, with mass $M_{500} = 8.09 \pm 0.49\ M_\odot$ and characteristic radius $R_{500} = 3.75'$. z = 0.41 corresponds to an angular distance of 1136 Mpc for the ΛCDM model, hence $R_{500} = 1.24$ Mpc in linear scale. PSZ2G243.15-73.84 has been observed in X-ray, as part of the the CHEX-MATE project, and in the radio band with the telescope MeerKAT. The cluster hosts a radio halo together with three radio relics positioned toward the eastern, western, and northern regions. All three relics exhibit a spectral index steepening with increasing distance from the cluster center. The radio halo power at 1.28 GHz is $P_{RH} = 3.89 \pm 0.18$ W/Hz, the central surface brightness is $I_0 = 0.566 \pm 0.025\ \mu$Jy/arcsec^2 and its dimension is $r = 316.7 \pm 40.2$ kpc. The properties of the three radio relics are summarized in the following table.

Relic	P_{RR} [W/Hz]	LLS [kpc]	DD_{cc-RR} [kpc]
West	15.89 ± 0.79	1131 ± 55	1229 ± 88
East	1.01 ± 0.05	813 ± 55	2235 ± 160
North	3.55 ± 0.18	635 ± 55	843 ± 61

Table 2.1: From left to right, the position of the radio relic, the radio relic power at 1.28 GHz, the largest linear size estimate of the relic and the distance from the center of the cluster.

In this work, PSZ2G243.15-73.84 was studied using MeerKAT polarisation observations in the L-band, 900-1670 MHz. The total bandwidth of the observation was 778 MHz, with lower edge at 890 MHz and central frequency of 1279 MHz. The band was divided into 1861 channels, each with a width of 418 kHz. The total observation time was 6 h 53 min. The center of the observation was at RA = 1 h 59 m 0.3 s and Dec = -34:14:06 degrees. The total field of view covered a portion of the sky of 3.68° × 3.68°. The expected theoretical noise for the observational setup was approximately 4.3 μJy/beam.

In addition to the radio data, X-ray observations from XMM-Newton (obtained as part of the CHEX-MATE project) were used for the analysis of PSZ2G243.15-73.84.

The total observation time was 14 h 36 m and covered energy band was 0.7-1.2 keV. From these observations, a count map, an exposure map, and an external background map were extracted, as in Bartalucci (2023) and Rossetti (2024).

Chapter 3

Imaging

3.1 Theory

3.1.1 Generics

The interferometer measures the Sampled Visibility V_s of the source, which corresponds to the product of the Visibility V_t and the Sampling Function III (a Dirac comb). The V_t (a complex function) is the Fourier Transform (FT, Eq.1.7.7) of the sky brightness distribution I_t of the source (Eq.1.7.10), but this is an ideal quantity, as the interferometer is only able to sample it through III (which is related to the (u, v) coverage: how the source sees the configuration of projected baselines constituting the interferometer).

To make an image of the source I_t it is necessary to reconstruct it starting from V_s, the observed u, v data. By masking V_s with 1 where it has a value and 0 where it has not, III can be obtained from V_s and, doing the FT^{-1} (Eq.1.7.8) on the latter, the Dirty Beam (DB) is derived. DB is the response to a point source. If instead a FT^{-1} is directly applied to V_s, the Dirty Map I_d is calculated. Notice that I_d is the result of the convolution between I_t and DB, analogues to V_s being the product between V_t and III in the Fourier space (real space: $I_t * DB \leftrightarrow$ Fourier space: $V_t \cdot III$).

$$\begin{array}{ccccc} I_t & * & DB & = & I_d(x,y) \\ FT\downarrow & & FT\downarrow & & FT\downarrow \\ V_t & \cdot & III & = & V_s(u,v) \end{array} \tag{3.1.1}$$

In order to obtain the image one must take the FT^{-1} of V_s to get the I_d and deconvolve it for the DB. I_d is an imperfect reconstruction of the sky due to the incomplete sampling of the uv plane. In the case of full uv sampling, the observation beam is Gaussian. However, if this is not the case, the beam exhibits sidelobes in addition to the main lobe, degrading the image quality. The deconvolution removes the sidelobes leaving only the main one. In practice the DB is substituted with the clean beam (CB), which is the elliptical Gaussian fit of the main lobe of the former. The deconvolution is done using the CLEAN algorithm.

3.1.2 Cell size

To generate an image from the visibilities using the CLEAN algorithm, the size of the pixels making the image must be specified . The image pixel size must be small enough to sample 2 times the FT of the longest baseline (size obtained using the Nyquist theorem). The sampling is done via a multiplication or convolution of III depending on the domain space. How much of the signal is recovered depends on the sampling rate chosen. In the Fourier space the operation of sampling creates replicas of the FT of the sampled function, and to not lose information such replicas must not overlap. In this case the sampled function is the FT of the $I_t = I_t(x, y)$ meaning $V_t = V_t(u, v)$, so the interested variables are x, y (spatial coordinate) and u, v (coordinate relative to the baseline). Here, only x and u are taken into consideration for simplicity's sake. The sampling theorem states that any continuous function extending up to the spatial frequency u_{max} may be reconstructed exactly from uniformly spaced samples separated in space by $1/\Delta x > 2u_{max} \rightarrow \Delta x < 1/2u_{max}$, the Nyquist rate. u_{max} is the longest baseline so $1/u_{max}$ is the angular resolution which is the beam, while Δx is the map pixel size. In practice, the pixel size is to be less than half of the beam, but is better to use 1/4 or 1/5:

$$\Delta x = \frac{1}{4}\frac{1}{u_{max}}. \tag{3.1.2}$$

Notice that in reality there are both the u and v coordinates so $u_{max} = \sqrt{u^2 + v^2}$ in the general case.

3.1.3 Cotton-Schwab CLEAN

The assumption of the standard cleaning algorithm is that each source is a collection of point sources, meaning that an extended source is the superposition of point sources. Among the various cleaning algorithms, this section discusses the Cotton-Schwab algorithm (Schwab, 1984), one of the fundamental algorithms. The cleaning algorithm is subdivided in two parts:
1) Clean

$$I^R(x, y) = I^D(x, y) - \gamma B(x, y) * I^C(x, y), \tag{3.1.3}$$

where $I^R(x, y)$ is the residual image, $I^D(x, y)$ is the dirty image, γ is the loop gain, $B(x, y)$ is the dirty beam and $I^C(x, y)$ are the clean components. Search for the brightest pixels in $I^D(x, y)$ to add them to the clean component list ($I^C(x, y)$) and convolve with the dirty beam. Subtract the list from $I^D(x, y)$ but just a part of the flux $\gamma = 0,1 - 0,3$. In this way $I^R(x, y)$ is created. Repeat once again with $I^R(x, y)$ being the new $I^D(x, y)$ until a stopping criteria is reached which can be:

- Max number of cleaning components to use in the cleaning process.
- $I^C(x, y) <$ multiple of the RMS (when RMS limited).
- $I^C(x, y) <$ fraction of the brightest source flux (when dynamic range limited).

2) Restore

$$I(x, y) = I^C(x, y) * B^I(x, y) + I^R(x, y), \tag{3.1.4}$$

where $I(x, y)$ is the clean ('final') image, $I^C(x, y)$ are again the clean components, $B^I(x, y)$ is the clean beam and $I^R(x, y)$ is the last produced residual image. Start from the last $I^R(x, y)$ and add back clean components convolved with $B^I(x, y)$.

The cleaning can be more complex having major and minor cycles, as follows:

1. Initialize the clean components $I^C(x, y)$.

2. Compute the dirty beam $B(x, y)$.
3. Compute the initial residual image $I^R(x, y)$.
4. While stopping criteria of major cycle is not reached
    (a) While stopping criteria of minor cycle is not reached
        i. Identify a new flux component in $I^R(x, y)$.
        ii. Update the clean components $I^C(x, y)$ and residual image $I^R(x, y)$:

$$I^R(x, y) = I^D(x, y) - \gamma B(x, y) * I^C(x, y)$$

    (b) Use the current clean components $I^C(x, y)$ to predict model visibilities.
    (c) Compute residual visibilities ($V_{\text{res}} = V_{\text{data}} - V_{\text{model}}$).
    (d) Compute $I^R(x, y)$ from residual visibilities.
5. Convolve the final clean components $I^C(x, y)$ with the clean beam $B^I(x, y)$ and add to the residual image $I^R(x, y)$:

$$I(x, y) = I^C(x, y) * B^I(x, y) + I^R(x, y)$$

The stopping criteria for the major cycle are the same as those described in "1) Clean": maximum number of iterations, RMS limit, and flux limit. The stopping criteria for the minor cycle requires that the peak falls below the level of the first side lobe in the initial residual image.

3.1.4 Multiscale CLEAN

There are several variations of the standard CLEAN algorithm. In multiscale CLEAN, the assumption that each source is a collection of point sources is relaxed to better recover extended emission. A CLEAN component is no longer limited to a single pixel, but can have a spatial extension. Following, the description of multiscale CLEAN as implemented in the **WSClean** software (Offringa and Smirnov, 2017):

1. Convolve the dirty image with a set of predefined scales of increasing size.
2. Identify the scale that contains the highest peak in brightness.
    (a) Locate the peak in the scale-convolved image.
    (b) Convolve this peak with the scale dependent beam and subtract it from the image.
    (c) Repeat the process until the initial peak falls below (1 − gain)× the new peak value.
3. Perform the Fourier Transform (FT) of the model image and subtract it from the visibility data.

3.1.5 Multifrequency CLEAN

When the bandwidth of the observation is large, it may result useful to divide the band in sub-bands when cleaning. In this way spectral information is taken into account during cleaning. Following, the description of multifrequency CLEAN as implemented in the **WSClean** software (Offringa and Smirnov, 2017):

1. Divide the band in sub-bands
2. Image each sub-band to create the dirty images via FT.
3. Begin the cleaning procedure:
    (a) Identify the brightest pixel to be subtracted by searching within the integrated image, which improves the signal to noise ratio (S/N). The position of this peak is then recorded.
    (b) At the same position, measure the flux density across all sub-band images.
    (c) Subtract a fraction (specified by the gain) of this flux, convolved with the corresponding dirty beam calculated for each sub-band.
4. Iterate this process until the peak brightness in the residual image falls below the threshold, as in the standard CLEAN algorithm.
5. The image of the full band is made by the weighted (for noise) average of the sub-bands images.

3.1.6 Weighting

Visibilities are weighted when going from the visibility plane to the image plane using a Fourier Transform (FT). There are several ways to weight, in most cases the parameter "robust" (ranging from -2 to 2) of the Briggs weighting scheme is used to control the weighting of the visibilities. The weighting is needed because the measured visibilities contain noise and some uv ranges are sampled more than others; typically short spacings are sampled more than long ones. The weighting is as follows: $V(u,v) = W(u,v)V'(u,v)$ where $V(u,v)$ is the visibility and $W(u,w)$ is the weight.

When robust is set to -2 the weighting is called uniform and the resolution is higher, meaning more sensitive to compact emission. In this case $W(u,v) = 1/d_s^2$, where d_s is the density of (u,v) points in a symmetric region of the uv plane, so the plane is more uniformly covered, resulting in better resolution. This kind of weighting will often utilize the data very irregularly, which in turn results in poor sensitivity.

If robust is set to 2 the weighting is called natural, and the resolution is lower, meaning sensitive to extended emission. In this case $W(u,v) = 1/\sigma^2$ where σ is the RMS, so the plane is less uniformly covered meaning a worse resolution. This weighting gives the best sensitivity.

3.1.7 W-gridding

When the FoV is sufficiently small the visibility function is

$$V(u,v) = \iint I'(l,m)e^{-2\pi i(ul+vm)}dldm. \tag{3.1.5}$$

When the FoV is large, the curvature of the sky cannot be neglected. A third coordinate, w, must be considered to take into account the normal direction with respect to the sky. The visibility function becomes

$$\begin{aligned} V(u,v,w) &= \iint \frac{I'(l,m)}{\sqrt{1-l^2-m^2}} e^{-2\pi i\left(ul+vm+w\left(\sqrt{1-l^2-m^2}-1\right)\right)}\, dl\, dm \\ &= \iint \frac{I'(l,m)\, e^{-2\pi i w\left(\sqrt{1-l^2-m^2}-1\right)}}{\sqrt{1-l^2-m^2}} \times e^{-2\pi i(ul+vm)}\, dl\, dm. \end{aligned} \tag{3.1.6}$$

For a small FoV it is a 2D FT

$$\frac{I'(l,m)}{\sqrt{1-l^2-m^2}} = e^{2\pi i w\left(\sqrt{1-l^2-m^2}-1\right)} \iint V(u,v,w) \times e^{2\pi i(ul+vm)} du dv, \tag{3.1.7}$$

where $e^{2\pi i w(\sqrt{1-l^2-m^2}-1)}$ is called w-term. Summing over $w_{max} - w_{min}$

$$\frac{I'(l,m)\,(w_{\max}-w_{\min})}{\sqrt{1-l^2-m^2}} = \int_{w_{\min}}^{w_{\max}} e^{2\pi i w\left(\sqrt{1-l^2-m^2}-1\right)} \times \iint V(u,v,w) e^{2\pi i(ul+vm)} du dv dw. \tag{3.1.8}$$

Meaning that to account for the w-term in wide field imaging, the sky function $I'(l,m)$ can be recovered by summing over the range $w_{\min}$ to $w_{\max}$ through the following steps:

1. Consider a region with approximately constant w.
2. Compute the FT^{-1} (inverse FT) of the visibilities within that w-slice.
3. Apply the phase shift
$$e^{2\pi i w(\sqrt{1-l^2-m^2}-1)}$$
to correct for the w-term.
4. Repeat steps 1-3 for all w-slices.
5. Sum the contributions from all slices.
6. Multiply by a final scaling factor proportional to
$$\frac{w_{\max}-w_{\min}}{\sqrt{1-l^2-m^2}-1}.$$

This procedure is known as w-stacking, which is the method implemented by **WS-Clean** (the name itself stands for "w-stacking clean"). In practice, however, the software uses w-gridding, a wide-field gridding algorithm similar to w-stacking. Instead of assigning each visibility to its nearest w-plane, w-gridding extends uv-gridding into the w-direction, distributing each visibility across a small range of w-planes, weighted by a kernel function.

3.2 Work

3.2.1 Application

The imaging process in this work was carried out using the **WSClean** software (Offringa et al., 2014). There are several ways to carry out imaging and this is reflected in the wide range of options provided by **WSClean**. A list of the used parameters to perform imaging is reported in Appendix A.1.
The "w-stacking" algorithm (more in Sec.3.1.7) was used to generate the initial total intensity (I) image. The max number of major iterations was set to 12, with a gain of 0.8. The stopping criteria during the CLEAN was to reach an emission level lower than 0.5 times the noise within the region with emission higher than 2.5 times the noise (for examples of successful multiscale cleaning, see Riseley (2022); Gan and Mertens (2023)). This region was selected using a mask generated through multiscale cleaning, with a threshold set at 2.5 times the noise level (Sec.3.1.4). The CLEAN components identified in this process were stored and used to create the emission mask (refer to Offringa and Smirnov (2017)). Within this mask, cleaning continued until 0.5 times the noise, as the masked region was confirmed to contain signal. The deep cleaning resulted in fewer undeconvolved residuals remaining in the image, improving the image quality. For the minor iterations the gain was 0.1. The image was composed by 11000 x 11000 pixels corresponding to a portion of the sky of 3.68° x 3.68°, with each pixel having size 1.2 arcsec (obtained with Eq.3.1.2). The Briggs robustness weight was set to -0.5, a compromise between uniform and natural weighting (refer to Sec.3.1.6). Multifrequency deconvolution was enabled (refer to Sec.3.1.5), with the total bandwidth being divided in 12 channels. A 2nd order polynomial was fitted through the channels measurements to smooth the spectrum. The **WSClean** command used to make this image is reported in Appendix B.1

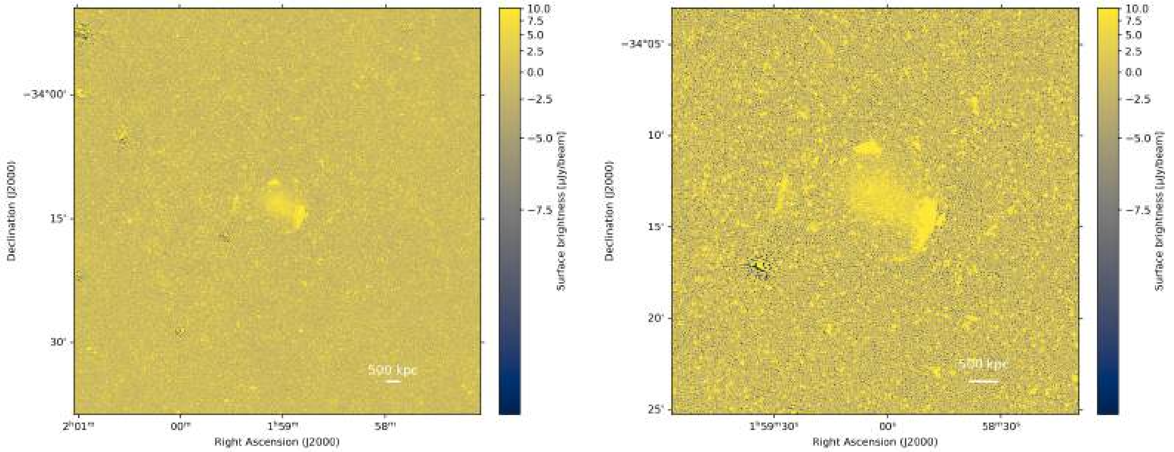

Figure 3.1: MeerKAT L-band Total intensity I images. Bandwidth = 778 MHz, central frequency = 1279 MHz, minor and major beam = 5.04″, noise ∼4.8 μJy/beam. Left panel image size = 0.82° x 0.82° (16.3 Mpc x 16.3 Mpc). Right panel image size = 0.37° x 0.37° (7.3 Mpc x 7.3 Mpc). These images are zooms of Fig.3.2. Images in Asinh scale.

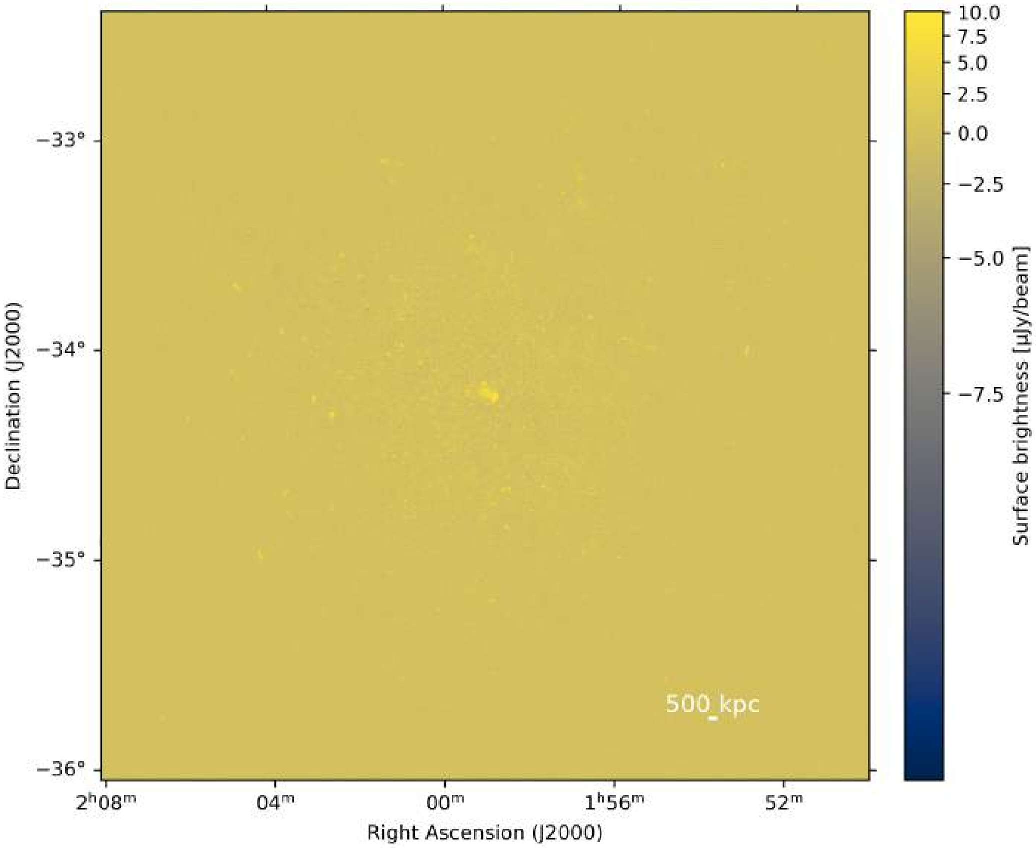

Figure 3.2: MeerKAT L-band Total intensity I image. Bandwidth = 778 MHz, central frequency = 1279 MHz, minor and major beam = 5.04″, noise ∼4.8 μJy/beam. FoV = 3.68° x 3.68° (73 Mpc x 73 Mpc). Image in Asinh scale.

The generated total intensity image is shown in Fig.3.2. Zoom-ins on the center of the FoV, where the galaxy cluster under study (PSZ2G243.15-73.84) is located, are shown in Fig.3.1. From largest to smallest (Fig.3.2, Fig.3.1 left panel and Fig.3.1 right panel) the size of the images are 3.68°, 0.82° and 0.37°, respectively 73 Mpc, 16.3 Mpc and 7.3 Mpc . The major beam and minor beam are 5.04″. The noise is ∼4.8 μJy/beam, comparable to the theoretical one, ∼4.3 μJy/beam. Beam correction was not, and will not be, applied in this work, as it does not affect the RM map or the polarisation fraction profile derived from the observations.

Chapter 4

Self-calibration

4.1 Theory

4.1.1 Generics

This section is based on the content presented in Taylor et al. (1999). It covers the basis self calibration, needed to follow Sec.4.2. The standard calibration equation is

$$\widetilde{V}_{ij}(t) = g_i(t)g_j^*(t)V_{ij}(t) + \epsilon_{ij}(t), \tag{4.1.1}$$

where $\widetilde{V}_{ij}(t)$ is the observed visibility between antenna i and j, $V_{ij}(t)$ is the true visibility, $g_i(t)$ & $g_j(t)$ are the complex gains for the array elements i and j, and $\epsilon_{ij}(t)$ is the thermal noise. During calibration $g_i(t)$ & g_j are determined using calibrators that may be located in a different part of the sky and observed at other times (see Sec.1.8), which can lead to residual errors. Consequently, calibrated data may still present amplitude and phase errors, which prevent from reaching the theoretical noise. This can lead to higher noise and to the presence of artifacts in the image.

A way to reduce the residual errors is by using self-calibration where complex gains become free parameters when determining the sky brightness distribution. Usually, this method is useful to improve the quality of the image when there are:

1. Extensive artifacts from the source of interest due to calibration errors
2. Extensive artifacts from a background source due to direction-independent calibration errors

Artifacts can be present in the image for several reasons. Generally, self-calibration works when the image contains sufficient flux, allowing the algorithm to improve the phase (and amplitude) solutions that were initially transferred from the secondary calibrator.

The procedure starts by creating a model for the sky brightness $\widehat{I}$ (e.g. by imaging the target visibilities) having $\widehat{V}$ as FT, which is the same as $\widetilde{V}_{ij}(t)$ once corrected for the complex gains. Minimization can be used to find $g_i(t)$ & $g_j(t)$ to reproduce $\widetilde{V}_{ij}(t)$. The sum of squares of residuals is

$$\mathcal{S} = \sum_k \sum_{\substack{i,j \\ i\neq j}} w_{ij}\left(t_k\right) \left| \widetilde{V}_{ij}(t)\left(t_k\right) - g_i\left(t_k\right) g_j^*\left(t_k\right) \widehat{V}_{ij}\left(t_k\right) \right|^2, \tag{4.1.2}$$

where $w_{ij}(t_k)$ is the weighting (inverse of the variance $\epsilon_{ij}(t_k)$). The time over which the complex gains are constant depends on the atmosphere. This would result in an overall iterative procedure:

1. Create a model of the source
2. Solve for the complex gains.
3. Compute the corrected visibilities $V_{ij,corr}(t) = \frac{\widetilde{V}_{ij}(t)}{g_i(t)g_j(t)}$
4. Create a new model from corrected visibilities
5. Restart until satisfied

4.1.2 Effectiveness conditions

Generally, self-calibration works best for arrays with many antennas, resulting in good (u, v) plane coverage. The requirement is to have less free parameters (complex gains and sky brightness model parameters) than (independent) visibility measurements. Self-calibration does not work when the signal to noise ratio is too low or the source is too complex, with respect the model. Furthermore, when applying self-calibration, features related to the undesired calibration errors must not be included in the model.

4.1.3 Established approach

In Eq.4.1.2, instead of solving for both phase and amplitude at the same time, only one can be addressed. Usually, starting by considering only phase and then both phase and amplitude is a good way to proceed.

4.1.4 Time averaging

While discussing Eq.4.1.2, it was mentioned that the time over which the complex gains remain constant depends on the noise and the atmosphere. Over this time $\widetilde{V}_{ij}(t)$ is averaged to improve the S/N. The best self-calibration interval is found by balancing the noise in the gain solutions with the real variability of the gains. Meaning, self-calibration is possible only if the gains vary more slowly than the time it takes to measure them with good S/N. Or in other words, the procedure works if the antenna can distinguish real signal from random noise before the atmosphere changes too much.

4.2 Work

4.2.1 Introduction

The total intensity (I) image shown in Fig.3.2 presents many artifacts, with similar shape and intensity scaling with the brightness (refer to Sec.4.1.1). In addition, the noise is higher than the theoretical one.

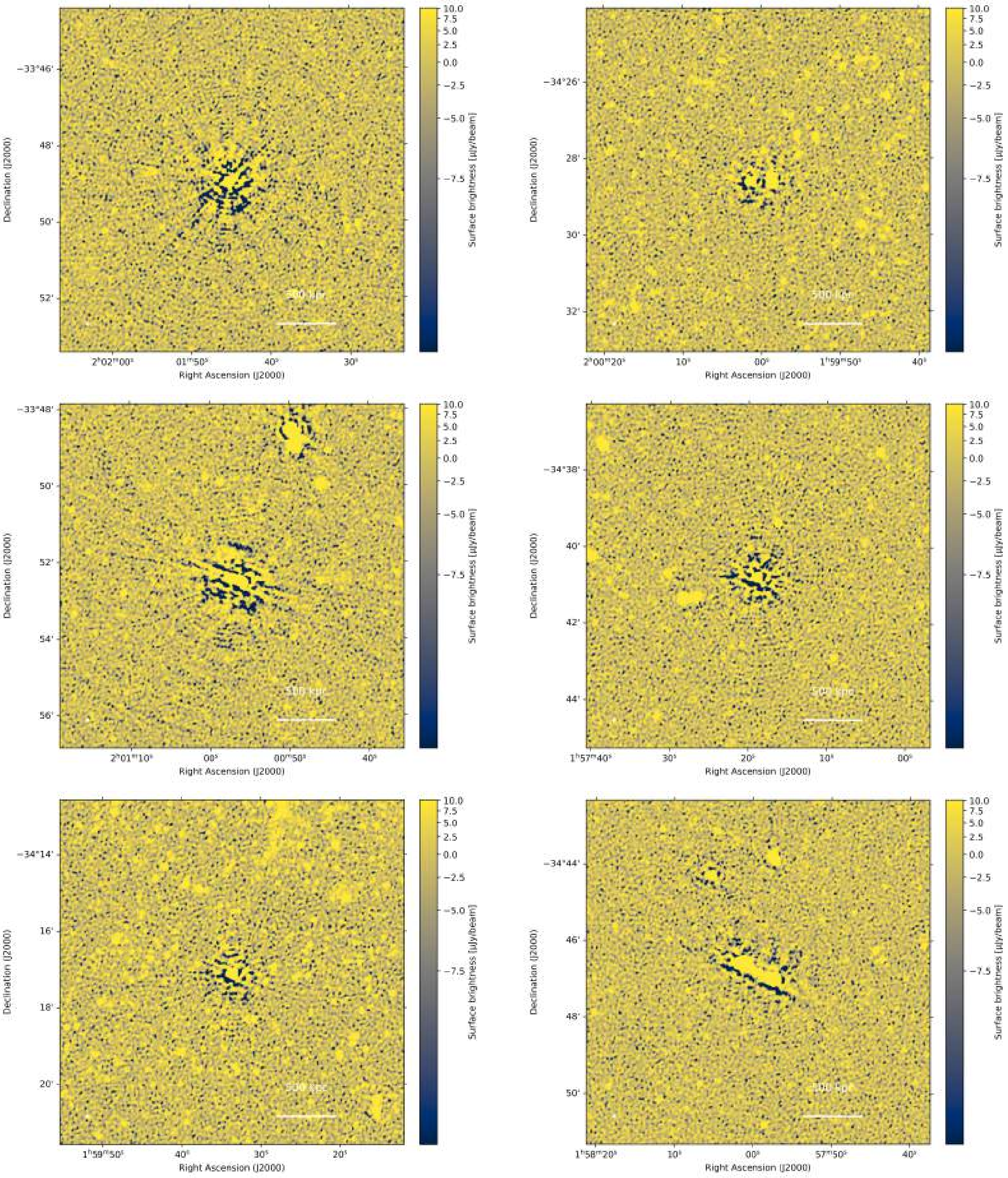

Figure 4.1: 6 of the artifacts present in Fig.3.2.

These were hints suggesting to use self-calibration to improve the quality of the image. The procedure was implemented through **facetselfcal.py** (van Weeren, 2021), which uses **WSClean** for imaging and the Default PreProcessing Pipeline, **DP3** (van Diepen, 2018), to find the complex gain solutions. A list of the used parameters to perform self calibration is reported in Appendix A.2.

4.2.2 Application

A total of 8 rounds of self-calibration were carried out on the data. During the first 4 rounds, only the phase was self-calibrated, while in the remaining 4, both phase and amplitude were considered (refer to Sec.4.1.3). For the rounds of only phase ("scalarphase") the solutions were computed every 2 minutes, while the time was increased to 5 minutes for the rounds of both phase and amplitude ("scalarcomplexgain"). At each iteration the default flagging strategy was applied to Stokes V to remove RFI (Radio Frequency Interference). When generating the images to be used as models with **WSClean**, the selected algorithm was "wstacking", the Briggs robustness weight was set to -0.5, multiscale and multifrequency deconvolution were enabled (bandwidth divided in 12 channels). To enforce smoothness over frequency, the solutions were convolved with a 100 MHz Gaussian kernel using **DP3**.

During the final self-calibration round, the extraction option was enabled, ensuring that clean components outside the chosen extraction region, defined with **DS9**, were not added back to the image. Consequently, the part of the image outside the extraction region remained without any signal. A square box with a side length of 0.33°, centered on the galaxy cluster (PSZ2G243.15-73.84), served as the extraction region. This corresponds to a physical size of 6.5 Mpc, sufficient to enclose the entire cluster given its virial radius of 1.24 Mpc.

The commands used for self calibration are reported in Appendix B.2.

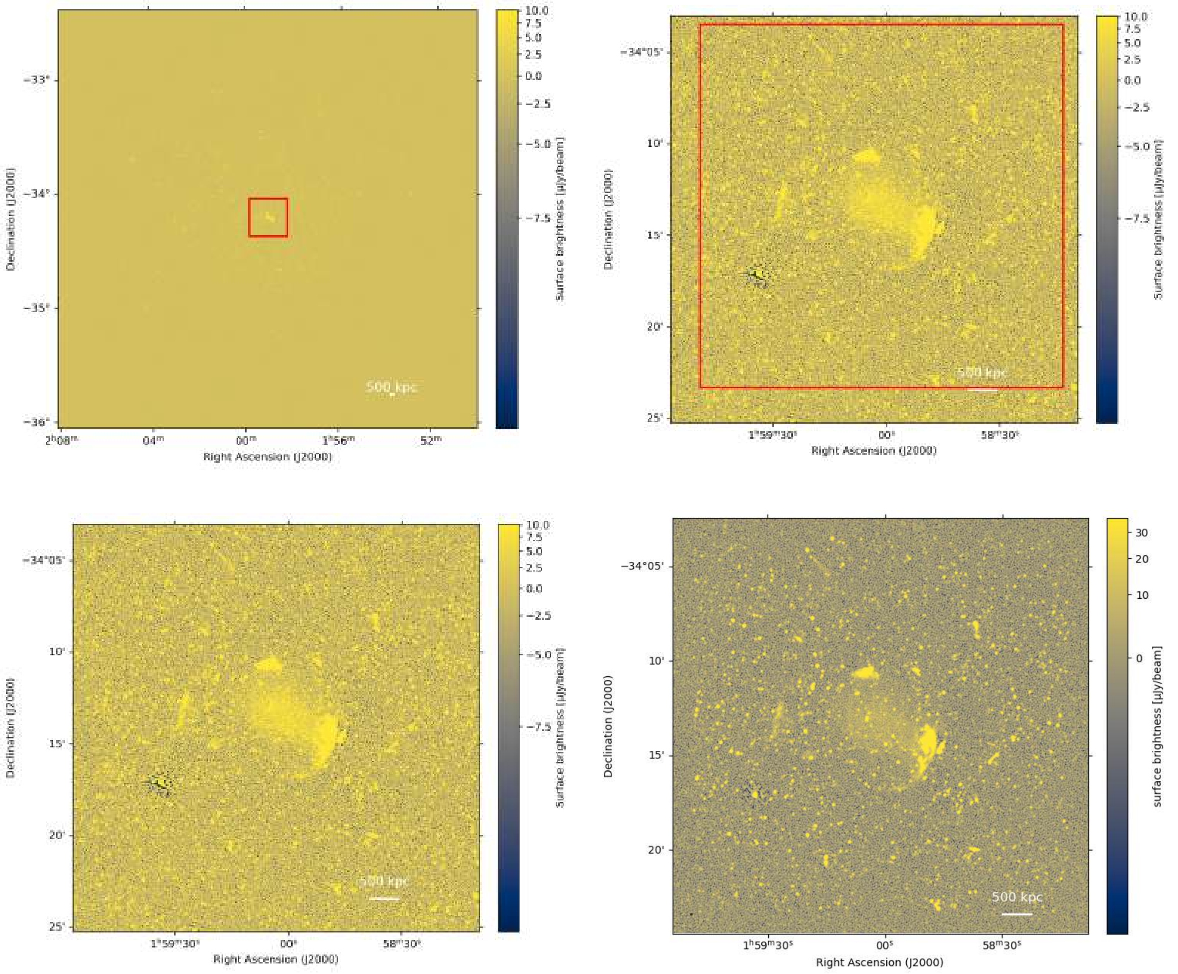

Figure 4.2: MeerKAT L-band total intensity images. Bandwidth = 778 MHz, central frequency = 1279 MHz. Top left panel: image before self-calibration, whole FoV 3.68° x 3.68° (73 Mpc x 73 Mpc), noise is ~4.8 μJy/beam, minor and major beam = 5.04″. Top right panel: zoomed in image of size 0.82° x 0.82° (16.3 Mpc x 16.3 Mpc) , in red the extraction region with size 0.33° x 0.33° (6.5 Mpc x 6.5 Mpc). Bottom left panel: zoomed in image with size 0.37° x 0.37° (7.3 Mpc x 7.3 Mpc). Bottom right panel: image after self-calibration with size 0.37° x 0.37° (7.3 Mpc x 7.3 Mpc), noise is ~4.3 μJy/beam, minor is 4.68″ while the major beam is 5.04″. Images in Asinh scale.

In Fig.4.2, four panels are presented. The top left panel shows the total intensity (I) image of the full FoV before self-calibration, which corresponds to the image in Fig.3.2. The small box in the center indicates the extraction region, with a size of 0.33° × 0.33° (6.5 Mpc x 6.5 Mpc). The top-right panel provides a zoomed-in view of the inner region, highlighting the extraction box in greater detail. This image has a size of 0.82° × 0.82° (16.3 Mpc x 16.3 Mpc). The bottom row compares the image before self-calibration (left) with that after self-calibration (right), both of size 0.37° x 0.37° (7.3 Mpc x 7.3 Mpc). The minor and major beam sizes before self-calibration were 5.04″, with the minor beam decreasing slightly to 4.68″ after self-calibration. The slight reduction in beam size occurred because some data, primarily from short baselines, were flagged during self-calibration. The image in the bottom right panel is the same shown in Fig.5.1.

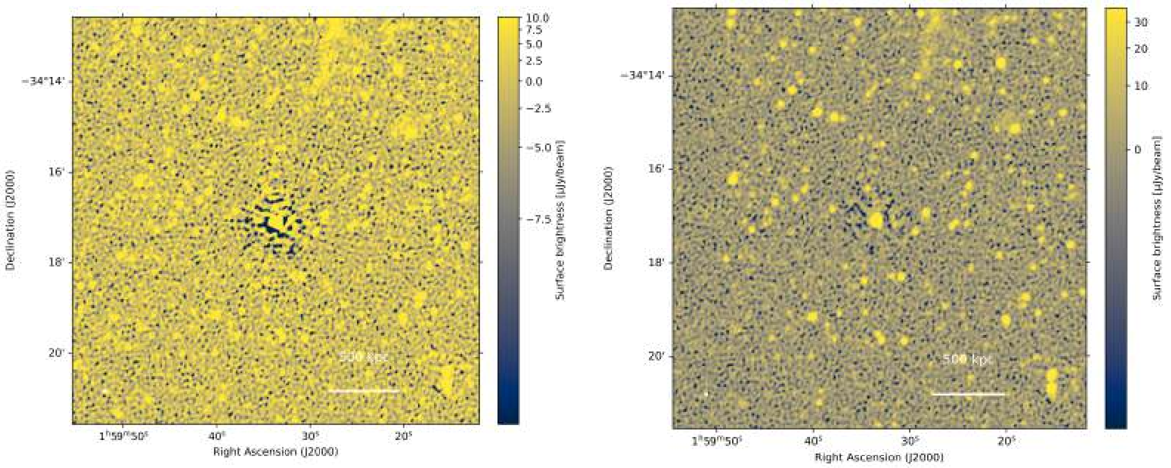

Figure 4.3: Left: pre self-calibration third artifact seen in Fig.4.1. Right: the same artifact post self-calibration visible in Fig.5.1. Images in Asinh scale.

Before self-calibration, the noise level was ∼4.8 μJy/beam. After the procedure, it decreased to ∼4.3 μJy/beam, in agreement with the theoretical prediction. Fig.4.3 shows how one of the artifacts became less prominent after self-calibration. A similar improvement was observed also for the others.

Chapter 5

Post self-calibration imaging

5.1 Total intensity imaging

After self calibration a new total intensity (I) image was generated similarly to the one shown in Fig.3.2. The differences are in the size and CLEAN algorithm. The image had a size of 1100 x 1100 pixels, equal to 0.37° x 0.37° (7.3 Mpc x 7.3 Mpc). So, slightly larger than the extraction region visible in the top right panel of Fig.4.2. In addition, multiscale deconvolution was enabled (refer to Sec.3.1.4), using scales of 0, 4, 8, 16, 32, 64, and 128 arcsec.

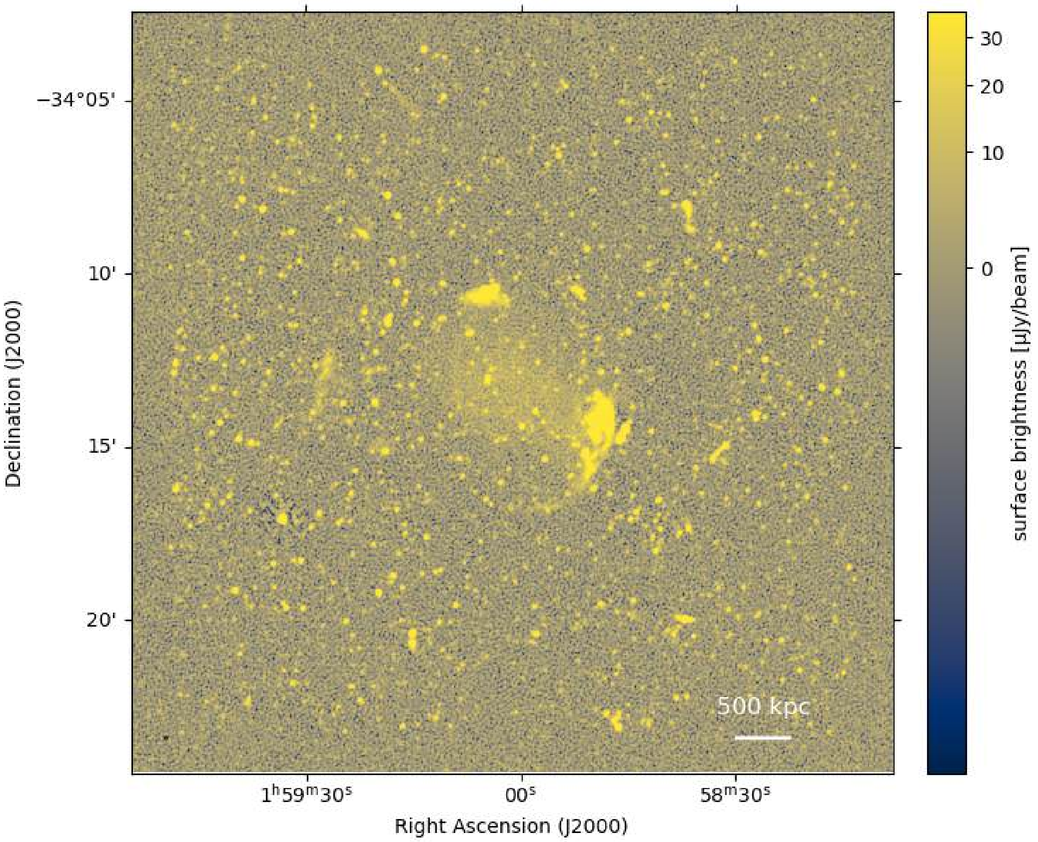

Figure 5.1: MeerKAT L-band total intensity (I). Bandwidth = 778 MHz, central frequency = 1279 MHz. Noise ~4.0 μJy/beam. Major beam = 5.04″, minor beam = 4.68″. Size 0.37° x 0.37° (7.3 Mpc x 7.3 Mpc). Image in Asinh scale.

The total intensity image (I) after self calibration is shown in Fig.5.1. Noise ~4.0 μJy/beam, major beam = $5.04''$ and minor beam = $4.68''$.

5.2 Polarised intensities imaging

The Stokes intensities U and Q were imaged in a slightly different manner with respect to the total intensity (I) image (shown in Fig.5.1). No polynomial fit was applied across the channels, in order to impose fewer constraints on the spectral shape of $Q(\nu)$ and $U(\nu)$. The number of out channel/sub-images was 186. This large number of channels was necessary to b able to perform RM-synthesis, ensuring that each channel was sensitive to the expected rotation measure values in galaxy clusters. RM-synthesis and its results are discussed throughout Sec.6.2. The use of RM-synthesis is necessary due to the presence of depolarisation effects, which reduce the observed polarisation fraction. In particular, since the Stokes images were generated using the full bandwidth, bandwidth depolarisation (discussed in Sec.6.1.2), reduces the U and Q intensities, lowering the polarisation fraction. Applying RM-synthesis corrects for this effect. The noise level in the Stokes Q and U images is expected to be similar to that in the total intensity I image (RMS_I). Consequently, the noise in each of the 186 channels was expected to be approximately $RMS_I/\sqrt{186}$. Therefore, the cleaning threshold for each channel was set as $3 \cdot RMS_I/\sqrt{186} \sim 0.847$ μJy. The cleaning was performed only in the portion of image selected via a total intensity (I) mask, which excluded the regions of the image where there was no I signal. Multifrequency cleaning was enabled and peak finding was performed in the Q and U sum over channels: $\sum_{ch} \sqrt{Q_{ch}^2 + U_{ch}^2}$.

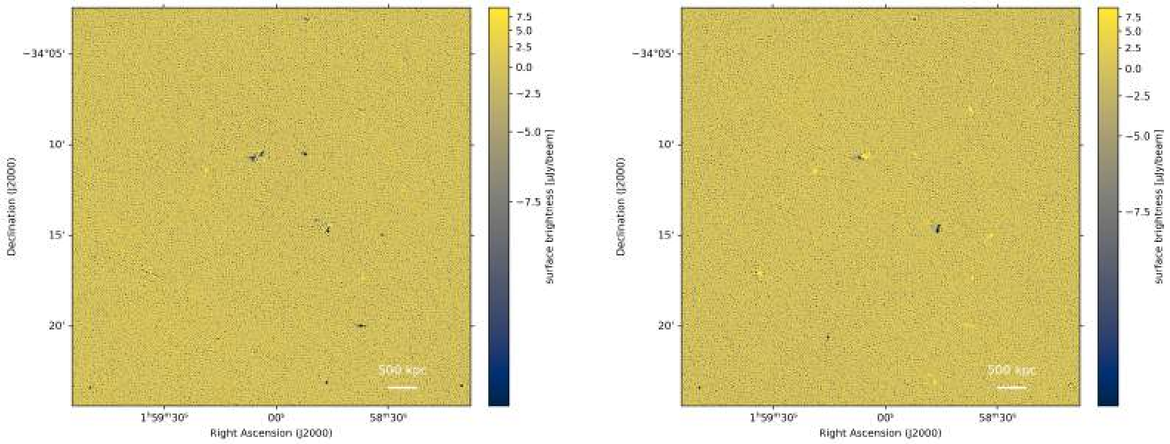

Figure 5.2: MeerKAT L-band polarised intensity images. Stokes Q in the left panel and Stokes U in the right panel. Bandwidth = 778 MHz, central frequency = 1279 MHz. Noise ~4.1 μJy/beam. Major beam = $4.68''$, minor beam = $5.04''$. Size 0.37° x 0.37° (7.3 Mpc x 7.3 Mpc). Images in Asinh scale.

The polarised intensities images are shown in Fig.5.2, where Q is on the left and U on the right. The major beam is $5.04''$, the minor beam is $4.68''$ and the noise for both images is ~4.1 μJy/beam. Polarised emission in the radio band originates from synchrotron radiation, which is linearly polarised. Therefore, Stokes V is zero (see Sec.1.5) and only the U and Q images were generated. The mask employed to CLEAN only the region showing total intensity (I) emission was created as follows:

1. Define a box with a specified width and height (in pixels).
2. Slide the box across the image.
3. Compute the local noise within each box position.
4. Identify pixels whose signal exceeds a chosen multiple of the local noise.
5. If no such pixels are found, mask out that region.
6. Repeat the process until the entire image has been covered.

The command used to create the Stokes U and Q images is reported in Appendix B.1.

Chapter 6

RM-synthesis

6.1 Theory

6.1.1 Faraday rotation

A magnetized medium characterized by a magnetic field B and a free electron density n_e behaves like a bi-refrangent medium with refractive index

$$n_{L,R} \approx 1 - \frac{1}{2}\frac{\omega_p^2}{\omega^2 \pm \omega\omega_L}, \tag{6.1.1}$$

where ω_p is the plasma frequency, ω_L is the Larmor frequency of the electrons and ω is the radiation frequency. For a linearly polarised wave, the two circular components of polarisation, left and right, feel different refractive indices, resulting in a rotation of the polarisation angle (Sec.1.6). This phenomenon is known as Faraday rotation.

Faraday rotation: the polarisation angle of linearly polarised emission rotates as the radiation propagates through a magnetized medium characterized by a magnetic field B and a free electron density n_e. The amount of ration depends on the wavelength λ of the emission

$$\Delta\psi = RM\lambda^2 \leftrightarrow \psi = \psi_0 + RM\lambda^2, \tag{6.1.2}$$

where RM is called rotation measure

$$RM = k\int_{los} B_{\parallel} n_e dl. \tag{6.1.3}$$

$B_{\parallel}$ is the component of the B along LoS (line of sight). Notice that the radiation, whose polarisation angle has been rotated, is generated outside the rotating medium. This takes the name of Faraday screen.

6.1.2 Bandwidth depolarisation

The total linear polarised intensity can be written as

$$P = pe^{i2\psi} = Q + iU, \tag{6.1.4}$$

where p and ψ are the amplitude and phase of the linear polarization vector, and adding the effect of the Faraday rotation

$$P = pe^{i2(\psi_0 + RM\lambda^2)} = pe^{i2\psi_0}e^{i2RM\lambda^2} = Q + iU. \tag{6.1.5}$$

The net result is a rotation of the polarisation.

A problem arises during observations due to the finite bandwidth. Since the rotation depends on the wavelength ($\propto \lambda^2$), the rotation angle does not rotate by the same amount over the bandwidth. At the edges of the band the difference in rotation is maximized. Assuming λ_0 & λ_{end} as limits of the band and $\lambda_0 \approx \lambda_{end}$:

$$\Delta\psi = RM(\lambda_0^2 - \lambda_{end}^2) = RM(\lambda_0 - \lambda_{end})(\lambda_0 + \lambda_{end}) \approx 2\bar{\lambda}\Delta\lambda RM = -c2\bar{\lambda}RM\frac{\Delta\nu}{\bar{\nu}}. \tag{6.1.6}$$

Thus, the polarisation vector rotates by different amounts across the bandwidth, and when averaged, its amplitude is reduced compared to what it would have been without Faraday rotation.

6.1.3 RM-synthesis generics

Consider now a magnetized medium with free electrons that emits linearly polarised radiation. At different depths within the medium, the generated radiation experiences a different RM. This concept is expressed by the Faraday depth

$$\Phi(\vec{r}) = k\int_0^{\vec{r}} n_e\vec{B}\cdot d\vec{r}, \tag{6.1.7}$$

so the total (linear) polarised intensity is

$$P(\lambda^2) = \int_{-\infty}^{+\infty} E(\Phi)P(\Phi)\cdot e^{i2\Phi\lambda^2}d\Phi, \tag{6.1.8}$$

where $E(\Phi)d(\Phi)$ is the fraction of the total emission between Φ and $\Phi + d\Phi$. Defining the Faraday dispersion function as $F(\Phi) = E(\Phi)P(\Phi)$, Eq.6.1.8 becomes

$$P(\lambda^2) = \int_{-\infty}^{+\infty} F(\Phi)\cdot e^{i2\Phi\lambda^2}d\Phi. \tag{6.1.9}$$

This relation can be inverted:

$$F(\Phi) = \frac{1}{\pi}\int_{-\infty}^{+\infty} P(\lambda^2)\cdot e^{-i2\Phi\lambda^2}d\lambda^2. \tag{6.1.10}$$

But in an observation $P(\lambda^2)$ is sampled only at some λ. This instrumental effect changes the $F(\Phi) \leftrightarrow P(\lambda^2)$ relation in to

$$F(\Phi)\bigstar R(\Phi) = \frac{1}{\pi}\int_{-\infty}^{+\infty} W(\lambda^2)P(\lambda^2)\cdot e^{-i2\Phi\lambda^2}d\lambda^2. \tag{6.1.11}$$

$W(\lambda^2)$ is the sampling function (indicating at which λ there are measurements), while $R(\Phi)$ is called RM transfer function ($RMTF$) and characterizes the instrumental response. The procedure of solving the RHS of Eq.6.1.11 to recover $F(\Phi)$ convolved with the $RMTF$ from $P(\lambda^2)$ is known as RM-synthesis (Brentjens and de Bruyn 2005). The sampling function is a limited box function, consequently the $RMTF$ is similar to a sinc function. The FWHM of the $RMTF$ gives the resolution for Φ of the observation

$$\delta_\Phi \sim \frac{2\sqrt{3}}{\Delta\lambda^2}, \tag{6.1.12}$$

where $\Delta\lambda^2 = \lambda_{end}^2 - \lambda_0^2$ and λ_0 & λ_{end} are the limits of the total bandwidth. In Sec.6.1.2 the problem of bandwidth depolarisation was introduced and it is still present when the bandwidth is divided in sub-channels. Therefore, there is a maximum observable Faraday depth for the channel due to depolarisation:

$$|\Phi_{\max}| \sim \frac{\sqrt{3}}{\delta\lambda^2}. \tag{6.1.13}$$

Where $\delta\lambda^2 = \lambda_{end}^2 - \lambda_0^2$ and λ_0 & λ_{end} are the limits of the channel.

6.1.4 Beam depolarisation

Consider polarised emission coming from a background source behind a magnetized medium containing free electrons. Due to Faraday rotation, the polarisation angle Ψ rotates within the beam. If the beam is small enough to separate regions of different magnetic field (B), the polarisation angle rotates by a constant quantity in each beam without decreasing the polarisation

$$P = pe^{i2\psi_0 + \Phi\lambda^2}, \tag{6.1.14}$$

this case takes the name of resolved Faraday screen. If the beam is not small enough to separate regions of different magnetic field (B), regions with different RM are mixed within the beam, leading ψ to not rotate as λ^2. This corresponds to the case of unresolved Faraday screen where depolarisation occurs

$$P\left(\lambda^2\right) = p_0 e^{-2K^2 \left\langle B_{\|} n_e \right\rangle_{\text{cell}}^2 dR\lambda^4}, \tag{6.1.15}$$

where R is the size of the cloud, B is the magnetic field, d is the size of cells where B varies and n_e is the electron density. Depolarisation for external Faraday screen takes the name of beam depolarisation.

6.1.5 Internal depolarisation

Internal Faraday depolarisation occurs when the medium that emits polarised radiation also rotates its own emission. As the radiation propagates through the magnetized plasma, its polarisation angle rotates according to Eq.6.1.2. Since the emission is generated at different depths along the line of sight, the amount of rotation depends on the position of the emitting region: radiation coming from the back side (with respect to the line of sight) of the plasma undergoes larger rotation than radiation coming from the front side. When integrating along the line of sight, polarised emission with different polarisation angles will partially cancel itself out, resulting in lower polarisation fraction. Observationally, internal depolarisation is identified by a wavelength dependent decrease in the polarisation fraction, which is distinct from beam depolarisation, and by deviations from a linear (λ^2) behavior of the polarisation angle for the Faraday screen. A detailed description and derivation for internal depolarisation can be found in Burn (1966) and Shneider (2014).

6.1.6 RM-clean

The result of the RM-synthesis is not the Faraday dispersion function ($F(\Phi)$) but its convolution with the rotation measure transfer function ($RMTF$), $F(\Phi)\bigstar R(\Phi)$. A deconvolving algorithm, RM-clean (Heald, 2009), can be applied to remove the side lobes of the $RMTF$ and recover the $F(\Phi)$:

1. Find the peak of the reconstructed Faraday dispersion function, Φ_p.
2. Scale the real and imaginary parts of $|F(\Phi_p) * R(\Phi_p)|$ by the loop gain g (typically $g = 0.1$) and record the result as a clean component.
3. Scale the $RMSF$ at Φ_p to $g||F(\phi_p)||$ and subtract it from the Faraday dispersion function.
4. Search for a new peak in the residuals and repeat the loop (scale, store, subtract and search) until a threshold (e.g. multiple of noise) or the max number of iterations is reached.
5. Restore the clean components using a Gaussian with a $FWHM$ approximately equal to the main lobe of the $RMTF$, and add this restored model to the residuals.

At the end the FDF deconvolved from the $RMSF$ is obtained.

6.2 Work

6.2.1 Introduction

Linearly polarised radiation originated inside or behind the galaxy cluster PSZ2G243.15-73.84 is subject to Faraday rotation (6.1.1). This meant that the MeerKAT observation was affected by bandwidth depolarisation (Sec.6.1.2). Therefore, the total (linear) polarised intensity was reduced. To solve the issue of bandwidth depolarisation, hence to recover the lost polarised intensity, the intention was to use RM-synthesis (Sec.6.1.3).

The choice of dividing the bandwidth in 186 channels, seen in Sec.5.2, was made considering RM-synthesis, which requires the full range of possible RM values. Since typical RM values in galaxy clusters are on the order of a few hundred $\mathrm{rad/m^2}$, and values up to about 1000 $\mathrm{rad/m^2}$ are observed at the centers of massive cool-core clusters, each channel was required to be able to detect at least 1600 $\mathrm{rad/m^2}$. The condition was imposed at the lower edge of the frequency band, where Faraday rotation is the strongest (see Eq.6.1.2). Eq.6.1.13 was used to determine how many observing frequency channels (in the lower edge of the band) were needed to observe at least a RM of 1600 $\mathrm{rad/m^2}$. With a starting frequency of 891 MHz and a (observing frequency) channel width of 418 kHz it was enough to group 10 observing frequency channels together to achieve the desired sensitivity to the RM, resulting in a final set of 186 channels.

RM-synthesis will take the 186 channels as input to determine and correct the RM responsible for the rotation of the polarised radiation, thereby recovering the polarised intensity lost due to bandwidth depolarisation.

The presence of a non-zero RM was also the reason to perform peak finding as $\sum_{ch} \sqrt{Q_{ch}^2 + U_{ch}^2}$ during the multifrequency cleaning seen in Sec.5.2. Without squaring Q and U, pixels with non-zero RM values would average out and would not be cleaned.

6.2.2 Beam selection

When performing RM-synthesis all the images must have the same beam. Consequently, all the 186 Q and 186 U images of the channels needed to be convolved to the same beam.

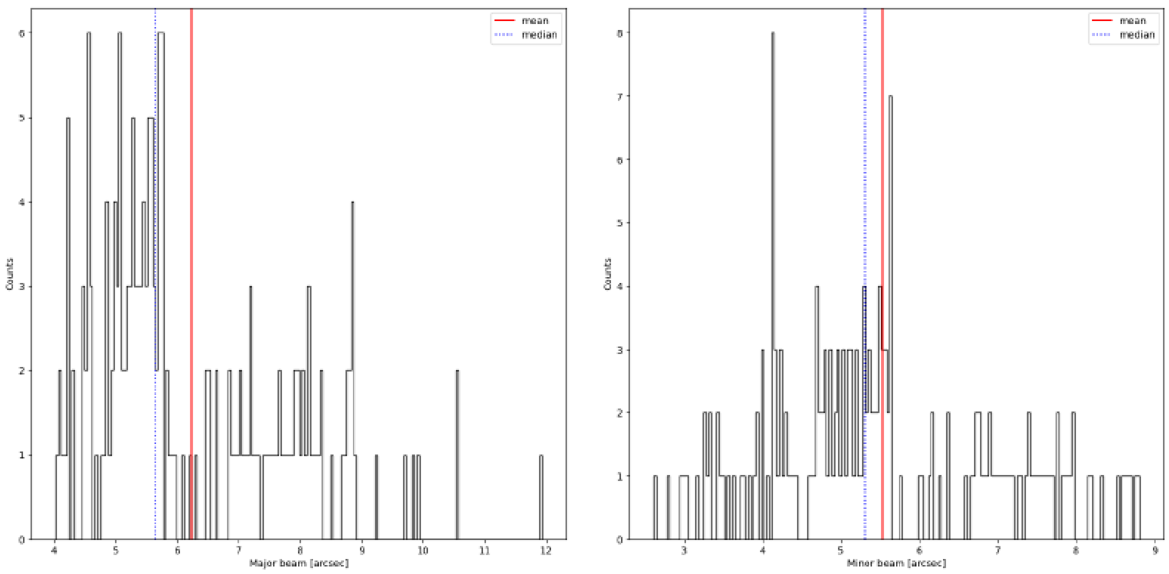

Figure 6.1: Left: Counts vs major beam in arcsec of the channels, red line is the mean of the major beams, dotted blue line is the median of the beams. Right plot is the same as left plot but with the minor beam.

In Fig.6.1, the histograms of the minor and major axis of the beams for the channels are shown. No outlying beams of large size were found. That is, no channel was discarded. Since all channels must be convolved to have the same beam, the presence of a significantly larger beam in one channel would be problematic, as all other channels would then need to be convolved to conform to it. In addition, such large beam size indicates that the channel is heavily flagged and should be discarded.

6.2.3 Noise selection

The noise level of all channels was examined to identify if any channel deviated significantly from the general behavior. Channels with anomalously high noise had to be discarded. The first found outlier was channel 12, whose noise was extremely high: 71697 μJy/beam in Stokes Q and 46629 μJy/beam in Stokes U. These values were far above the corresponding mean noise levels of 437 μJy/beam and 301 μJy/beam, respectively.

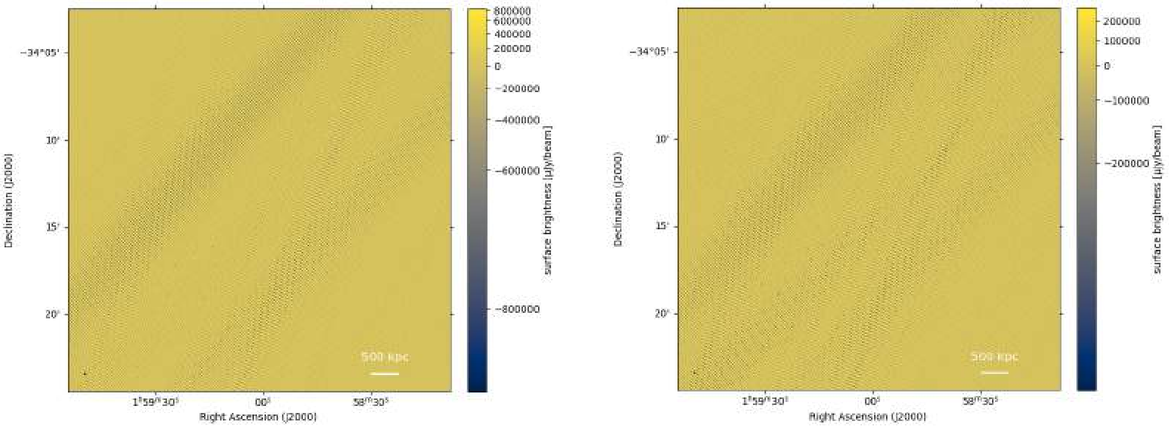

Figure 6.2: Left: Q image of channel 12. Right: U image of channel 12.

In Fig.6.2 the images of the outlying channel are shown, Q on the left and U on the right. The signal seemed to be dominated by a precise baseline but no further investigation was carried out.

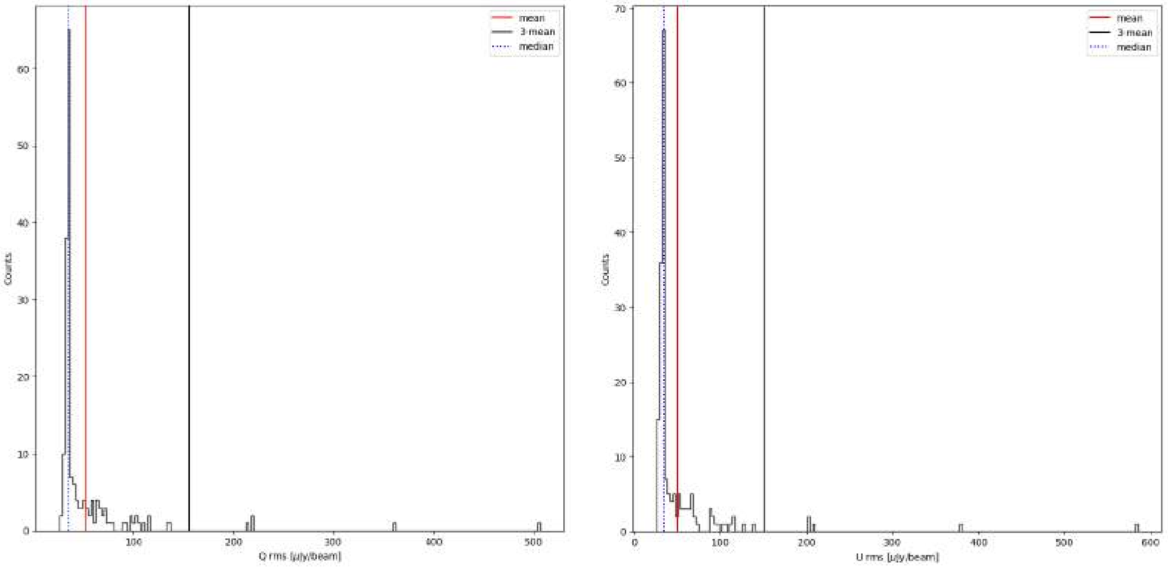

Figure 6.3: After channel 12 removal. Left: Counts vs noise of the channels for Q images, red line is mean noise $= 51.89$ μJy/beam, dotted blue line is the median noise $= 35.12$ μJy/beam. Right plot is the same as left plot but for U images, mean noise $= 50.35$ μJy/beam, median noise $= 33.87$ μJy/beam

In Fig.6.3 the histograms for the noise of the Q and U images of the channels are shown, after channel 12 was discarded. All channels with a noise greater than 3 times the mean noise were discarded, for Q this lower cut was at $3{\cdot}51.89$ μJy/beam while for U it was at $3{\cdot}50.35$ μJy/beam. 5 channels were removed (channels number 11, 67, 68, 69 90).

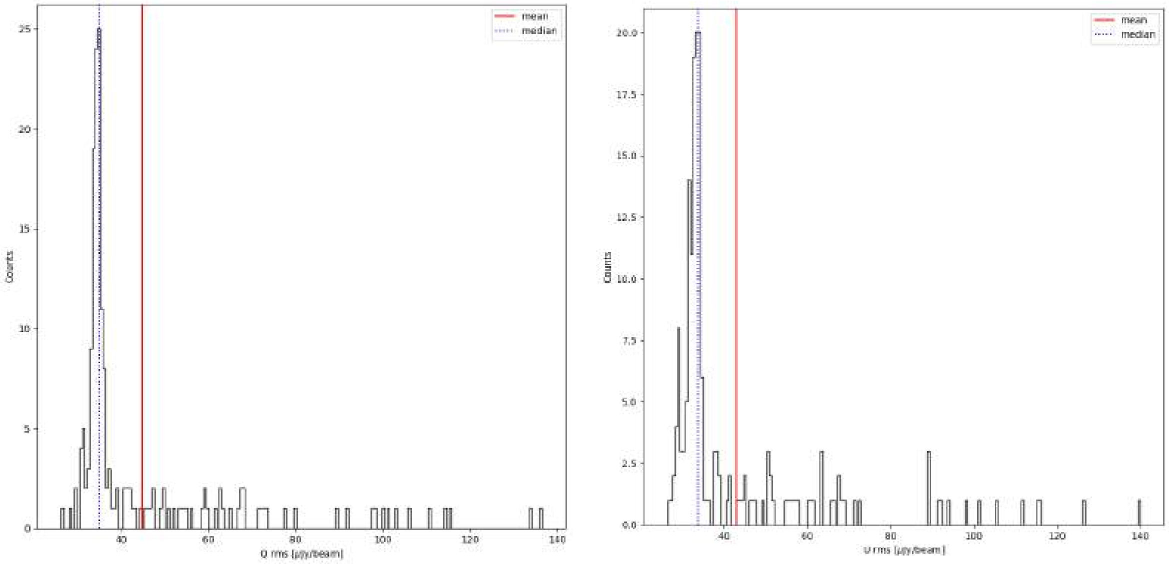

Figure 6.4: After noise selection. Left: Counts vs noise of the channels for Q images, red line is mean noise $= 44.89$ μJy/beam, dotted blue line is the median noise $= 35.05$ μJy/beam. Right plot is the same as left plot but for U images, mean noise $= 42.99$ μJy/beam, median noise $= 33.72$ μJy/beam

In Fig.6.4 the histograms for the noise of the Q and U images of the remaining channels are shown. The remaining 180 channels will be used during the RM-synthesis.

6.2.4 Convolution

When performing operations between images, the beam must be the same. This was valid for the RM-synthesis taking in as input the Q and U images of the channels. All 180 Q images, 180 U images and the total intensity (I) had to be convolved to have the same beam size. The method **imsmooth** of the software **CASA** was used to perform a Fourier-based convolution over all the cited images (CASA tutorial, 2021).

Using **imsmooth**, an image I can be smoothed to a target resolution by convolving it with a Gaussian beam B_{targ}. If the image is already convolved with another smaller beam B_{cur} (beam of the observation), a correcting beam B_{cor} can be calculated so that $B_{tar} * I = B_{cor} * (B_{cur} * I)$. The Fourier transform is $B^f_{tar} I^f = B^f_{cor}(B^f_{cur} I^f)$ and then the correcting beam can be obtained by $B_{cor} = F^{-1}(B^f_{tar}/B^f_{cur})$.

14.4″ was set as the target resolution, slightly larger than the maximum beam size among the channels (11.9″). Since both the major and minor beam axes were convolved to the same size, the resulting beam was circular.

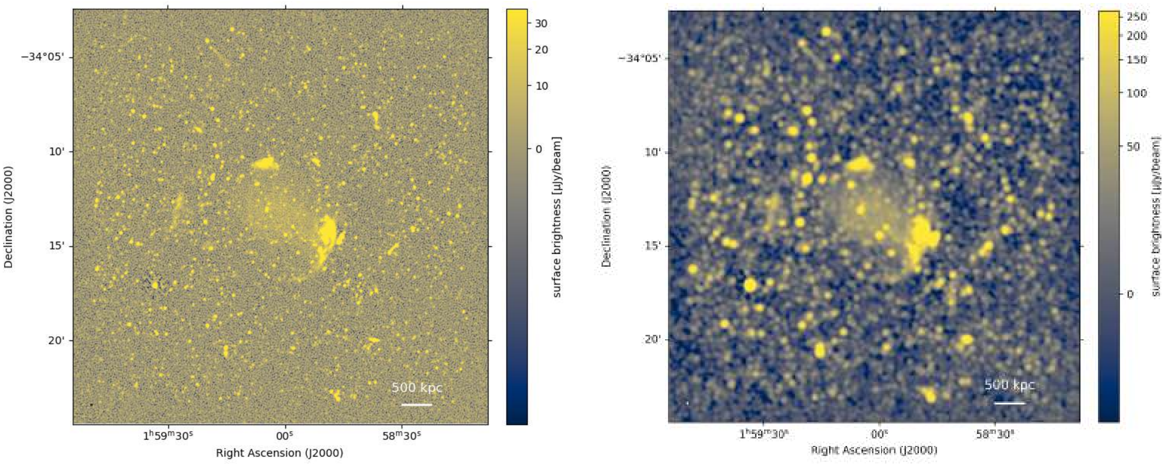

Figure 6.5: MeerKAT L-band total intensity (I) images of PSZ2G243.15-73.84. Left: same image shown in Fig.5.1. Right: left panel image after being convolved to have minor beam = major beam = 14.4″, noise ∼5.6 μJy/beam. Images in Asinh scale.

In Fig.6.5 the total intensity images (I) before and after convolution are shown. In the left panel, the original image with a resolution ∼5.04″. In the right panel the same image after convolution is shown, now with a resolution of 14.4″. Also, all the Stokes U and Q images were convolved to this same resolution.

6.2.5 RM-synthesis application

The RM-synthesis was used to solve for bandwidth depolarisation (Sec.6.1.2). This was performed using the software **RM-Tools** (Purcell, 2020). The U and Q images were grouped and used to create the U and Q cube needed for the synthesis. Notice that the cubes were not uniformly spaced because some channels were discarded due to their high noise. Using Eq.6.1.12 the FWHM of the rotation measure transfer function ($RMTF$) was found to be ∼43 rad/m^2. The Faraday dispersion function (FDF, seen in Sec.6.1.3), also called Faraday depth spectrum, was calculated between -2000 and 2000 rad/m^2 and with a spacing of 2 rad/m^2 symmetrically around zero. The lowest frequency channel was sensitive to RM around 1600 rad/m^2, while the highest-frequency channel was sensitive to RM around 2000 rad/m^2. Hence, by using the range -2000,2000 rad/m^2, part of the spectrum remains free of signal and can be used to obtain a precise estimate of the noise of the FDF. Each channel was weighted with the inverse square of the Stokes Q and U error. Using these values, the theoretical noise expected for the FDF was estimated to be ∼1.8 μJy/beam by computing

$$\sigma_p = \frac{1}{\sqrt{\sum_{ch} \frac{1}{RMS_{ch}^2}}} \tag{6.2.1}$$

where σ_{ch} is the noise of the single channel.

The RM is a quantity integrated along the LoS, as shown in Eq.6.1.3. The Q and U images were made of 1100 x 1100 pixels, each corresponding to a different LoS. Therefore, RM-synthesis produced 1100 x 1100 FDF spectra, one for each pixel.

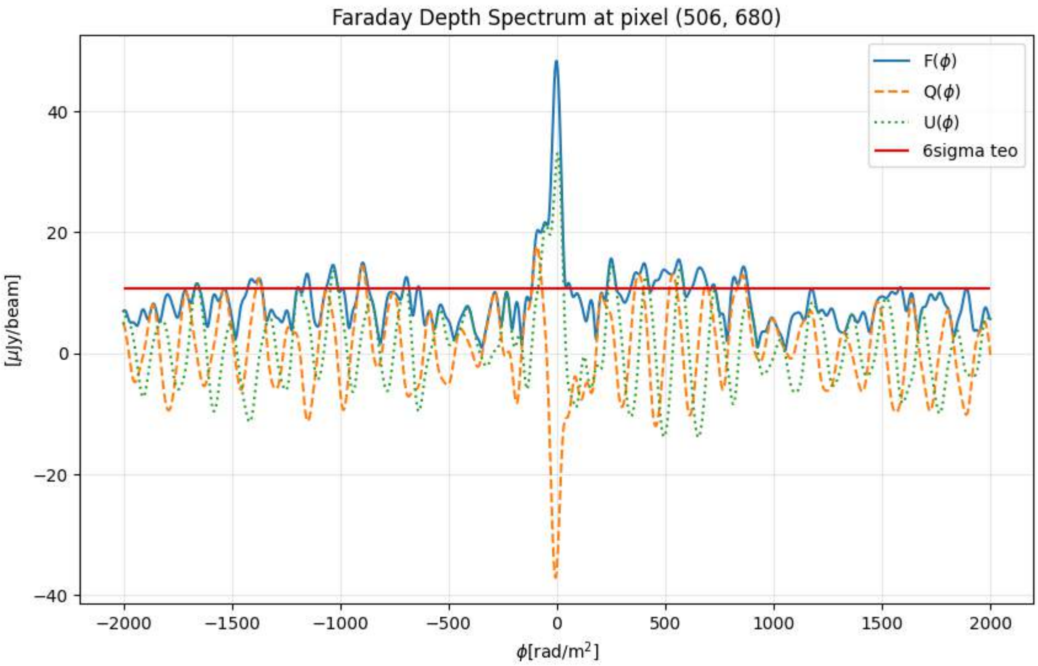

Figure 6.6: FDF of a pixel in the northern relic, with coordinates RA = 1h 59m 6s and Dec = -34:10:50 degrees. Dashed orange line is Stokes Q, dotted green line is Stokes U, continuous blue line is the total polarised intensity F and the red horizontal line is 6 times the noise σ_P computed in the edges of the ϕ range, in [-2000,-1800] and [1800,2000] rad/m^2.

The FDF of a pixel positioned in the center of the northern relic, having RA = 1h 59m 6s and Dec = -34:10:50 degrees, is shown in Fig.6.6. The dashed orange line is the Stokes Q intensity, the dotted green line is the Stokes U intensity, the continuous blue line is the total polarised intensity F and the red horizontal line is 6 times the noise σ_P. The noise was computed in the edges of the ϕ range, in [-2000,-1800] and [1800,2000] rad/m^2, where there should be no or little signal. In this case, the peak of the spectrum was higher than 6 times the noise (σ_P), indicating that the pixel contained polarised signal. The height of the FDF's peak is the total polarised intensity. A threshold of $6\sigma_P$ was defined to distinguish signal from noise. This choice is motivated by the fact that $6\sigma_P$ corresponds approximately to a 5σ Gaussian significance level (Hales, 2012). Pixels with an FDF peak exceeding this value were considered to contain polarised signal, while those below it were classified as noise. Notice that each pixel had its own spectrum, thus its own σ_P. The mean σ_P across all pixels was ~2.6 μJy/beam, slightly higher than the theoretical value, ~1.8 μJy/beam. The FDF showed a single dominant peak, indicating that the Faraday rotation occurs in a screen external to the emitting source. This is consistent with the case of polarised emission passing through an external Faraday screen. The same behavior was observed for the other pixels containing signal.

6.2.6 RM-clean application

The FDF was disentangled from $RMTF$ using RM-clean (Sec.6.1.6), implemented through the software **RM-Tools**. The threshold was set as 3 times the theoretical noise σ_p. Another possibility was to use the mean noise of the FDF spectra, but the theoretical one was preferred due to being slightly lower, which allowed a deeper cleaning.

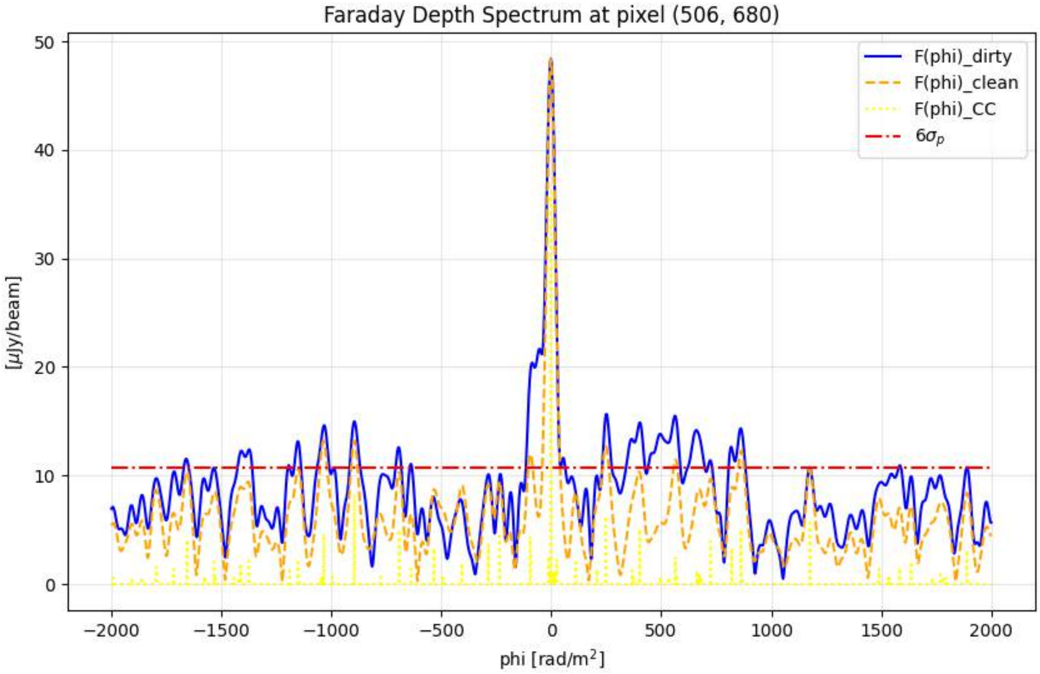

Figure 6.7: FDF of a pixel in the northern relic with coordinates RA = 1h 59m 6s and Dec = -34:10:50 degrees, after cleaning. Dashed orange line is the FDF before the clean, dotted yellow line are the clean components, continue blue line is the FDF after clean and the red horizontal line is 6 times the noise σ_P for the clean FDF computed in the edges of the ϕ range in [-2000,-1800] and [1800,2000] rad/m^2.

After the cleaning there was no significant change in any of the FDF, they still indicated the presence of a single RM and so of a single external Faraday screen. In Fig.6.7 the FDF pre and post clean for the same pixel of Fig.6.6 are shown. The CLEAN procedure deconvolved the spectrum to remove the instrumental response and therefore helped to better delineate the underlying spectrum. A secondary peak was visible to the left of the main one, rising only slightly above the $6\sigma_p$ level. Given its marginal significance, especially with respect to the main peak, it did not provide any additional information for the analysis. The RM-clean did not provide any meaningful additional insight for the FDF of any pixel.

6.2.7 Results

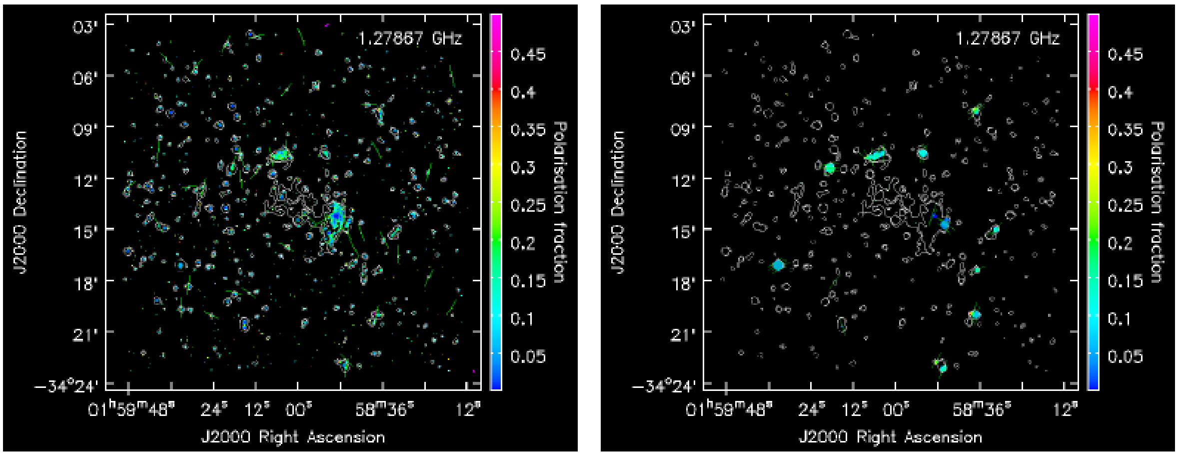

Figure 6.8: Left: polarisation fraction image pre RM-synthesis, masked at 5 times the total intensity image noise and 6 times the total polarised intensity image noise. Bandwidth = 778 MHz, central frequency = 1279 MHz, major beam = 5.04″ (27.8 kpc) and minor beam = 4.68″ (25.8 kpc). The green lines are the polarisation vectors tracking the orientation of the magnetic field. In white the total intensity contour levels at 9 and 18 times the I noise. Right: polarisation fraction image post RM-synthesis, masked at 5 times the total intensity image noise and 6 times the noise of the FDF for each pixel. Same parameters as in the left panel, except for major and minor beam axis = 11.4″ (62.8 kpc) (images went through convolution). Polarisation vectors are rotated to their original position and corrected for the RM of the Milky-Way.

The polarisation fraction images obtained before (left) and after (right) RM-synthesis are shown in Fig.6.8. In white the total intensity contour levels at 9 and 18 times the I noise. The polarisation fraction image in the left panel was derived combining the Stokes U and Q intensities images (seen in Fig.5.2) by doing $\sqrt{U^2 + Q^2}$, then dividing for the total intensity image I (Fig.5.1). Notice that the image on the left has the original resolution, with major beam of 5.04″ (27.8 kpc) and minor beam of 4.68″ (25.8 kpc), whereas the image on the right has resolution of 11.4″ (62.8 kpc). The polarisation fraction in the right panel was computed with the result of the RM-synthesis. For each pixel the height of the FDF peak gave the amount of total polarised intensity. An image of these peak values, corrected for Ricean bias using $P = \sqrt{FDF_{peak} - 2.3\sigma_p^2}$ (George, 2013), was then created. Dividing this image by the total intensity (I) image produces the polarisation fraction image. This time, all the used images were convolved to have beam = 11.4″ x 11.4″ (62.8 kpc x 62.8 kpc)). The locations of the FDF peaks also provided the rotation measure (RM) along each line of sight, allowing the corresponding RM map to be constructed, which will be shown (Fig.8.6) and discussed later on.

The pre RM-synthesis image was masked at 5 times the total intensity (I) image noise and 6 times the total polarised intensity (P) image (the one created by doing $\sqrt{U^2 + Q^2}$) noise. The post RM-synthesis was masked in I as the other image, but the criterion for the cut in total polarised intensity was different. The noise of the total polarised intensity was computed for each pixel based on its FDF spectrum. Each pixel had to exhibit an FDF peak at least six times higher than its corresponding FDF noise.

The right image was the result of RM-synthesis. Twelve polarised sources were present and all showed a FDF with a single peak, indicating that the observed Faraday rotation occurs in a screen external to the source. Two of them spatially correspond to the north and eastern relics, but their FDF still presented a single peak. This is likely due to beam depolarisation and internal depolarisation. In addition to the 12 sources, there were many scattered pixels around the whole image.

In both images the polarisation vectors are shown, indicating the orientation of the magnetic field. The post RM-synthesis vectors were corrected for the Faraday rotation, and also the Milky-Way RM was subtracted from them.

Unfortunately, the majority of the image did not contain signal. Consequently, the idea of comparing the observed RM map with a simulated one to derive information about the magnetic field had to be discarded. Hence, the focus remained only on the polarisation fraction profile.

Chapter 7

X-ray analysis

7.1 Surface brightness profile

The Miró code requires a density cube to generate a simulated *RM* map, so a corresponding density profile must be derived. To recover this profile, X-ray observations were analyzed with the aid of the software **pyproffit** (Eckert, 2020).

The X-ray data of PSZ2G243.15-73.84 were taken with XMM-Newton for the CHEX-MATE project. From these observations, a count map, an exposure map and an external background map were extracted (as in Bartalucci (2023) and Rossetti (2024)). In the count map, 79 sources and areas with zero exposure were excluded. 2D spline interpolation was used to fill the empty gaps left behind. In addition, a Poisson realization was generated for the spline interpolated data, to ensure that the filled holes had statistical properties consistent with the neighboring areas. The count map was then divided by the exposure map to obtain the surface brightness image in units of [counts/seconds/arcmin^2].

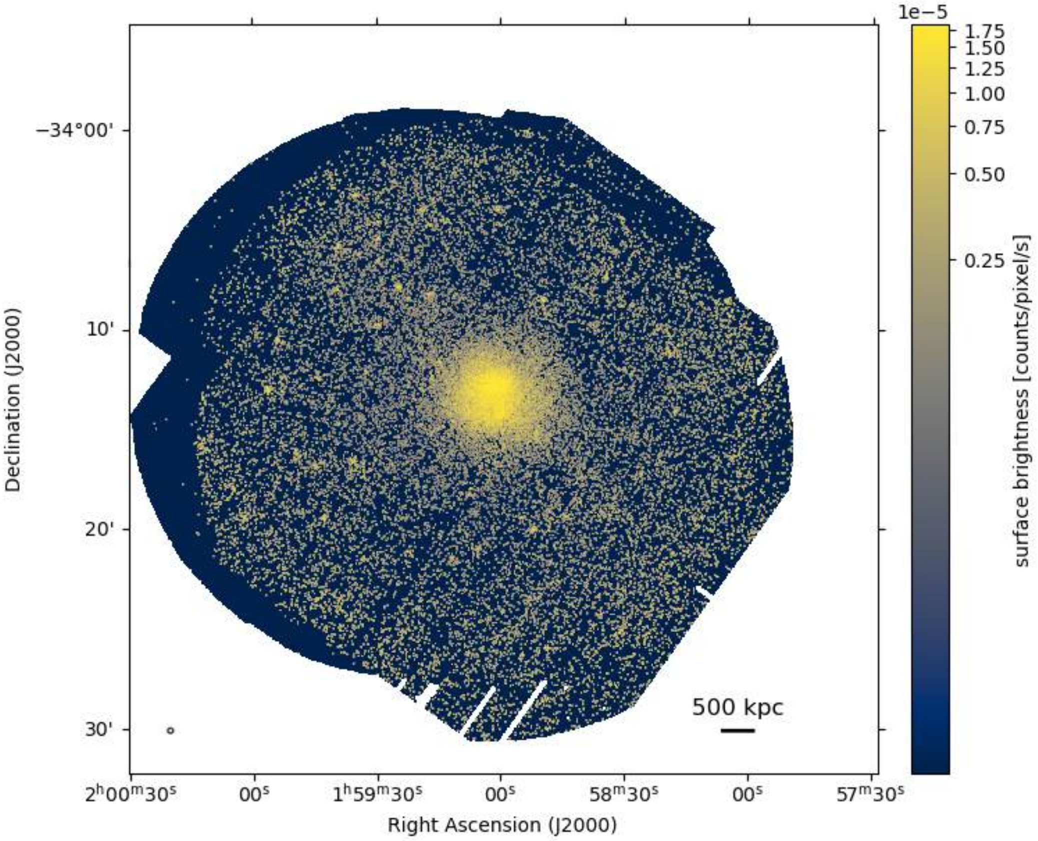

Figure 7.1: XMM-Newton X-ray surface brightness image of PSZ2G243.15-73.84. Covered area of the sky is 37.5′ x 37.5′ (12.4 Mpc x 12.4 Mpc), the dimension of a pixel is 2.5″, the energy range is 0.7-1.2 keV, PSF around 12″. Image in Log scale.

The X-ray surface brightness image is shown in Fig.7.1. The covered area of the sky is 37.5′ x 37.5′ (12.4 Mpc x 12.4 Mpc at the cluster redshift) and the dimension of a pixel is 2.5″. The 0.7-1.2 keV band was selected, as it maximizes the signal-to-noise ratio of the cluster's thermal emission (Ettori (2010)). The PSF of the observation is approximately 12″.

The surface brightness profile was extracted from this image. The extraction was performed in elliptical annuli centered on the image centroid, with position angle (of the ellipse from the right ascension axis) and the axis ratio (major/minor) determined via principal component analysis. The peak of X-ray emission was found to be in right ascension = 01h 59m 02s and declination = -34°13'16". The extraction reached a distance of 10.5′ (3.5 Mpc) from the center with bin size of 2.4″ (13.2 kpc).
The profile was fitted with a β model

$$I(r) = I_0 \left(1 + \left(\frac{x}{r_c}\right)^2\right)^{-3\beta+0.5} + B, \tag{7.1.1}$$

where x is the radius in arcmin, β is the beta parameter, r_c is the core radius, I_0 is the log of central surface brightness (whose units are counts/s/arcmin^2) the normalization and B is the log of the background (also in counts/s/arcmin^2).

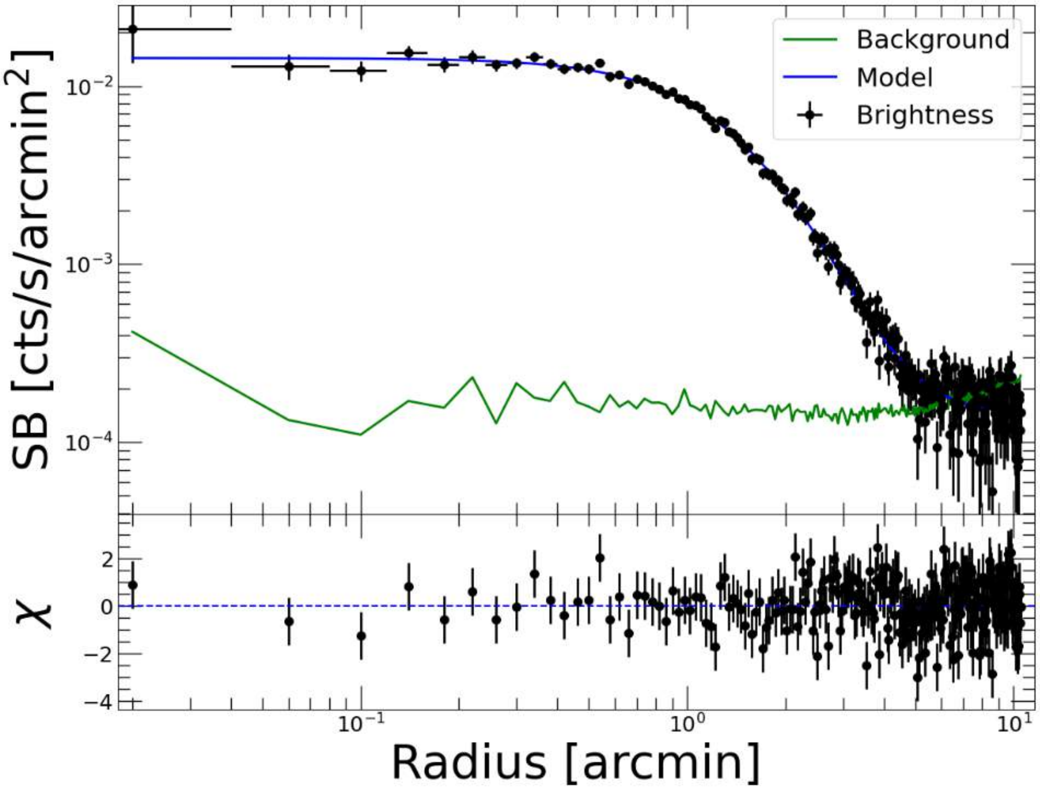

Figure 7.2: X-ray surface brightness fitted with a β model. In black the data points extracted from the X-ray image (Fig.7.1), in blue the fitted β model and in green the background.

The data points of the extracted X-ray surface brightness profile and its fit with a β model are shown in Fig.7.2. In black the data points extracted from the X-ray image (Fig.7.1), in blue the fitted β model and in green the background. r_c was found to be $1.95' \pm 0.07'$, β was 0.996 ± 0.034, I_0 was -1.846 ± 0.008 and B was -3.837 ± 0.015. The best fit chi-squared was 281.1 for 263 bins and 259 d.o.f (degrees of freedom), therefore the reduced chi-squared was 1.09.

7.2 Deprojection

The density profile can be recovered from the deprojection of the surface brightness profile. The method used was multiscale, implemented with **pyproffit**.

The multiscale deprojection, described in Eckert (2016), is a fitting procedure of the surface brightness or the emission measure to retrieve the density profile. The emission measure (EM) is given by

$$\mathrm{EM}(s) = \int n_e^2(r)\, dl, \tag{7.2.1}$$

where n_e is the electron density and l is the length of the emitting region on the LoS. When using the multiscale approach, the emission measure (EM) is fitted with a combination of N King functions that can be independently deprojected

$$EM(s) = \sum_{i=1}^{N} A_i \left(1 + \left(\frac{s}{r_{c,i}}\right)^2\right)^{-3\beta_i + 0.5} \tag{7.2.2}$$

where $r_{c,i}$ are the core radii, s is the projected cluster centric distance, A_i are the normalizations and β_i are the slopes. Normalizations and slope are the parameters left to vary when fitting. The King function is the deprojection of the β model often used to describe the density of galaxy clusters. Therefore, n^2 can be expressed as the sum of the deprojected king function, meaning β models

$$n^2_{\mathrm{gas}}(r) = \sum_{i=1}^{N} n^2_{0,i} \left(1 + \left(\frac{r}{r_{\mathrm{c},i}}\right)^2\right)^{-3\beta_i} . \tag{7.2.3}$$

The density is obtained from the fit parameters A_i and β_i, with A_i being linked to $n^2_{0,i}$.

$$n^2_{0,i} = \frac{\Gamma(3\beta)}{\Gamma(3\beta - 0.5)\sqrt{\pi} r_{\mathrm{c},i}} A_i, \tag{7.2.4}$$

where Γ is the Euler Gamma function. The multiscale procedure can be summarized as follow:

1. Start from a basis of β models for the density, with fixed core radii and free normalizations and slopes.
2. Project each one into its respective King function
3. Combine the King function to obtain the EM.
4. Fit the derived EM to the observed one.
5. Deproject the king functions into β models
6. Combine the β models to retrieve the density profile.

The multiscale approach works as long as

1. The gas density is smooth and decreases with increasing radii. That is, there are no sources strong enough to create bumps in the profile.
2. Gas density is always positive. Meaning, the background is subtracted correctly.

Prior to deprojection, point spread function (PSF) deconvolution and modeling were applied to the surface brightness profile to correct for PSF smearing. To achieve this, a PSF mixing matrix, describing the leakage of photons between annuli, had to be created. The XMM-Newton PSF was modeled as a King function with a core radius of 5.3″:

$$f_{\mathrm{King}}(r) = \left[1 + \left(\frac{r}{r_0}\right)^2\right]^{-\alpha} , \tag{7.2.5}$$

where r_0 is 5.3/60 arcmin and α is 1.59. For each annulus, a normalized image was generated, convolved with the PSF via a Fast Fourier Transform (FFT), and the fraction of events in the resulting convolved image that remained within each annulus was calculated to build the mixing matrix (each one of its rows represent the fraction of events originating from that annulus that are detected in the other rows). Finally, this matrix was used to correct for PSF smearing.

To proceed with the multiscale method, the redshift z and the conversion factor (cf) were required. The redshift is known, $z = 0.410$, while cf was computed using **XSPEC** by simulating an absorbed APEC (Smith, 2001) model with an emission measure (EM) of 1 and extracting the corresponding count rate (CR). cf is the conversion factor between X-ray surface brightness and EM. Note that surface brightness usually refers to the physical quantity, while CR corresponds to the measurement recorded by the instrument. The difference between the two lies in the correction for the instrumental response. However, in Sec.7.1, surface brightness was used synonymously with the count rate, representing the direct measurement from the instrument. So, the link between EM and CR or surface brightness is given by

$$\mathrm{EM}(s) = \mathrm{cf} \times \mathrm{CR}(s). \tag{7.2.6}$$

The X-ray surface brightness is

$$S_X(s) = \frac{1}{4\pi(1+z)^4} \int n_e^2(r)\, \Lambda(T, Z)\, dl, \tag{7.2.7}$$

where z is the redshift, n_e is the electron density, Λ is the cooling function, T is the temperature and Z is the metallicity. Hence, the emission measure (Eq.7.2.1) represents only one component of the surface brightness, while the conversion factor (cf) accounts for the remaining dependencies on the redshift (z) and the cooling function $\Lambda(T, Z)$.

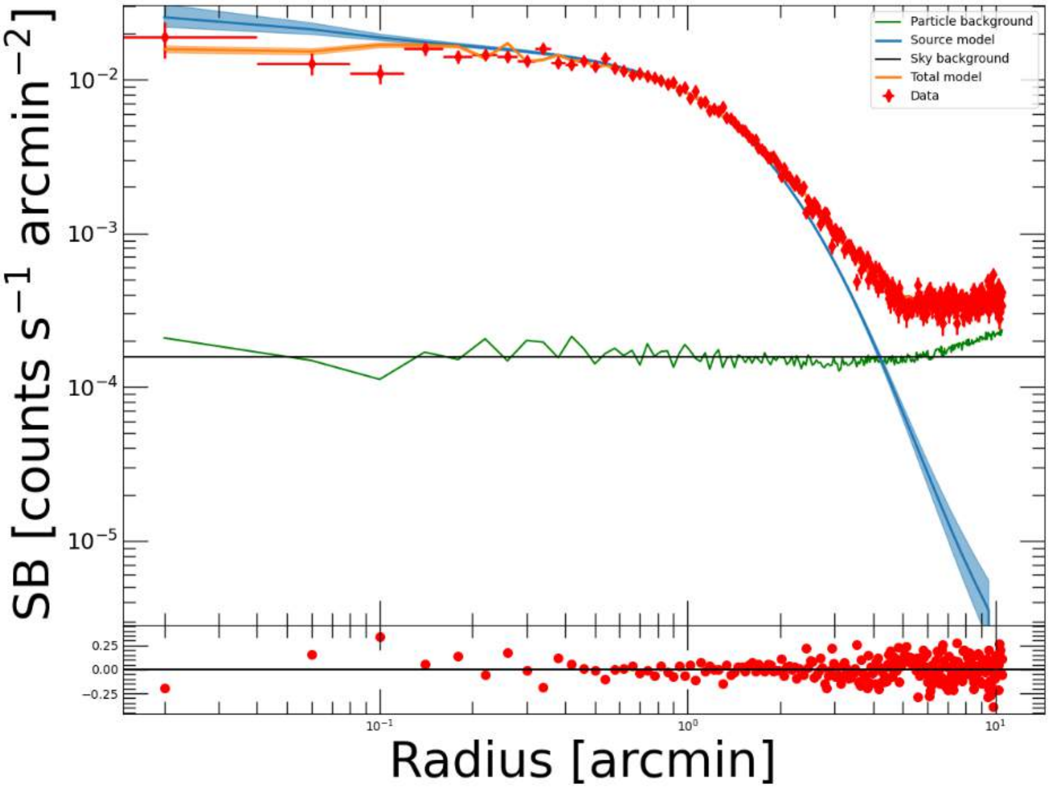

Figure 7.3: X-ray surface brightness fitted with a combination of β models during the multiscale processes. In red the data points extracted from the X-ray image (Fig.7.1), in blue the fitted β model, in green the particle background and in blue the source surface brightness.

The X-rays surface brightness fitted during the multiscale process is shown in Fig.7.3. In red the data points extracted from the X-ray image (Fig.7.1), in blue the fitted β model, in green the particle background and in blue the source surface brightness.

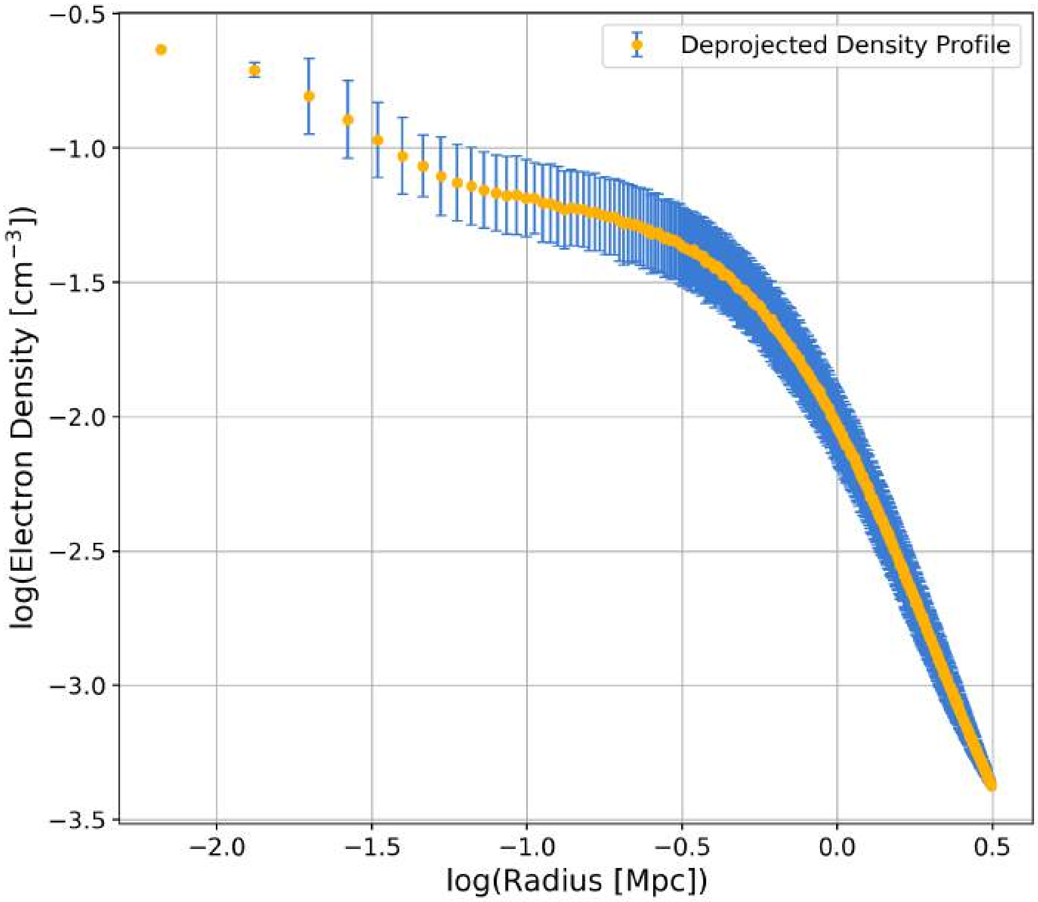

Figure 7.4: Log-log plot of the density profile deprojected from X-ray surface brightness through multiscale.

The density profile obtained from the multiscale, deprojection analysis is shown in Fig.7.4. The extension and binning are the same as in the surface brightness profile seen in Fig.7.3. The error was rescaled from the standard deviation of the surface brightness to have the same relative uncertainty. In the considered 0.7-1.2 keV band, the X-ray emissivity is almost independent of the gas temperature (Ettori, 2010). In addition, variations in the gas density profile are expected to be significantly more important than those in the temperature. Thus, it was reasonable to assume that the uncertainties in the surface brightness directly traced those in the density. The density profile was used to generate a density cube where the peak is at the cluster center coordinates and at the halfway point through the LoS axis. The cube was filled with densities having a Gaussian scatter, and to avoid negative extracted values, the error was reduced so that 3 times the standard deviation remained positive to avoid unphysical negative values.

Chapter 8

Simulations

8.1 MirRó code

The MiRó code produces an RM map from a supplied density and magnetic field cube. A detailed description of the code can be found in Bonafede (2013) and Stuardi (2021).

The density cube may be provided externally or generated internally using a model such as the β-mode or the universal gas density profile found by Ghirardini (2019) analyzing a sample of galaxy clusters.

The magnetic field is constructed following the power spectrum described in Domínguez-Fernández (2019), which is based on cosmological MHD simulations

$$E_M(k) = Ak^{3/2}\left[1 - \mathrm{erf}\left[B\ln\left(\frac{k}{C}\right)\right]\right], \tag{8.1.1}$$

where $k = \sqrt{\sum_{i=1}^{3} k_i^2}$ is the wavenumber associated with the physical scale of the magnetic field fluctuations. The size of the cube sets the minimum wavenumber (the largest physical scale that can be represented), while the maximum wavenumber (corresponding to the smallest physical scale) is determined by the Nyquist criterium. A gives the normalization of the magnetic spectrum, $B = 1.054$ is related to the width of the spectra, and $C = 4.354$ Mpc^{-1} is the wavenumber corresponding to the peak of the spectrum. For these values of B and C the power spectrum peak is at ∼230 Kpc. The minimum scale for the magnetic field is two pixels. To generate a divergence-free magnetic field with the chosen power spectrum, the corresponding spectrum for the vector potential $\tilde{A}(k)$ in Fourier space is adopted (Murgia (2004) and Tribble (1991)). For each pixel, the amplitude $A_{k,i}$ of the three components is drawn from a Rayleigh distribution with scale parameter $E_A(k)$, while the phase of each component is selected uniformly in the range $[0, 2\pi]$. This procedure ensures that the resulting magnetic field components follow a Gaussian distribution. The magnetic field in Fourier space is then given by

$$\tilde{\mathbf{B}}(\mathbf{k}) = i\,\mathbf{k} \times \tilde{\mathbf{A}}(\mathbf{k}), \tag{8.1.2}$$

which satisfies the divergence-free condition and reproduces the desired power spectrum. The field $\tilde{\mathbf{B}}(\mathbf{k})$ is subsequently transformed into real space through an inverse Fast Fourier Transform (FFT). The resulting magnetic field $\mathbf{B}$ has components B_i drawn from a Gaussian distribution with $\langle B_i \rangle = 0$ and variance $\sigma_{B_i}^2 = \langle B_i^2 \rangle$. The radial profile of the magnitude of the magnetic field is expected to scale with the thermal electron density (Domínguez-Fernández (2019), Bonafede (2010a) and Murgia (2004))

$$B = B_0 \left(\frac{n_e}{n_0}\right)^{\eta} \quad , \quad \beta = \frac{n_e k_B T}{B^2/8\pi}, \tag{8.1.3}$$

where B_0 is the magnetic field at the center of the cluster, n_0 is the density at the center, β (β parameter) is the ratio of the gas and magnetic field energy density, T is the temperature and n_e is the electron density. The magnetic field is scaled according to the density profile and then normalized to the mean field value B_{mean} within R_{500}. B_{mean} also sets the value of the parameter A in Eq.8.1.1.

Once the magnetic-field cube and gas-density profile has been generated, the RM map can be obtained by numerically integrating Eq.6.1.3 along one axis (one axis of the cube).

8.2 Observed polarisation fraction profile

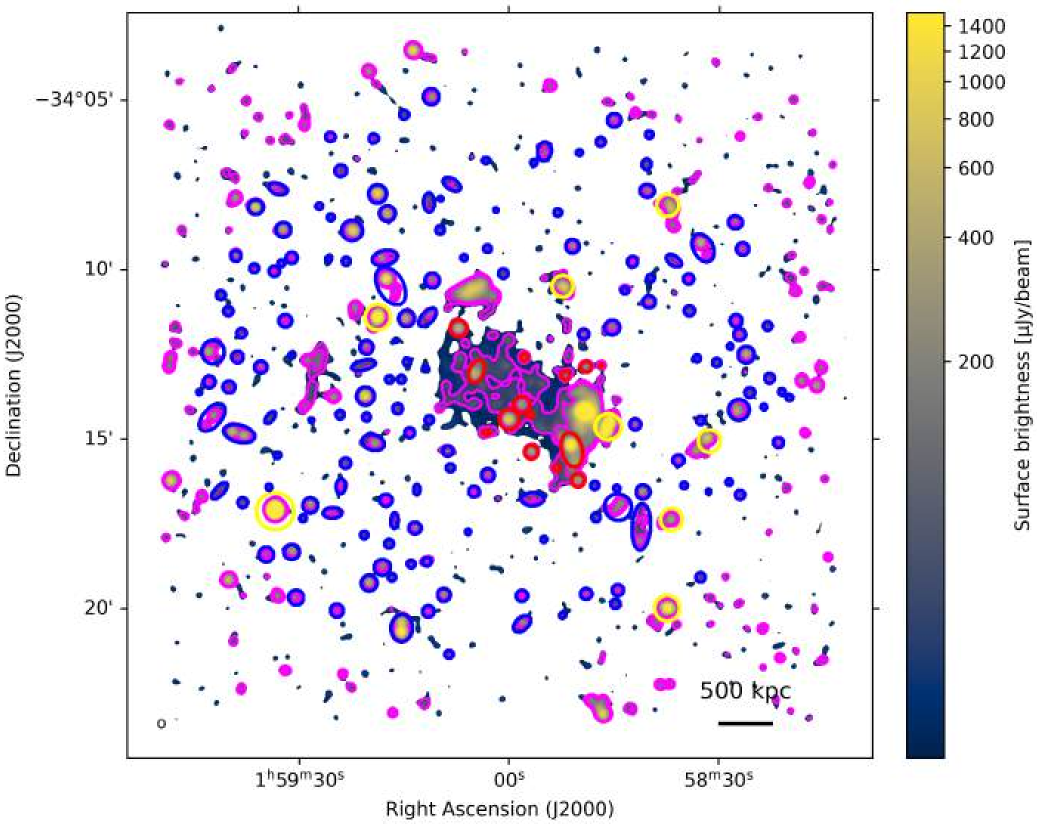

Figure 8.1: MeerKAT L-band total intensity (I) image of SZ2G243.15-73.84. Minor beam = major beam = 5.04″, noise ∼5.6 μJy/beam. Image masked at 5 times the noise. In blue the regions of total intensity emission, in red regions of total intensity emission in the same L.o.S. as the radio halo, in yellow regions of polarised intensity emission, in magenta the total intensity contour levels at 9 and 18 times the I noise. Image in Asinh scale.

The total intensity I image masked at 5 times the noise is shown in Fig.8.1. In the figure, the regions of total intensity emission are shown in blue, the regions of total intensity emission along the same line of sight as the radio halo are shown in red, the regions of polarised intensity emission are shown in yellow, and the total intensity contour levels at 9 and 18 times the I noise are shown in magenta. The synthesized beam has a size of $5.04'' \times 5.04''$ and the noise level is $\sim$5.6 μJy/beam. The regions were selected following the contours levels at 9 and 18 times the I noise. The radio halo was excluded since it is affected by internal depolarisation, and the relics were excluded because they are foreground sources whose Faraday rotation does not pass through the cluster. These regions were selected to create a polarisation fraction and RM profiles. Regions with not enough pixel to cover a beam of the observation were discarded, since they could not even be considered point sources.

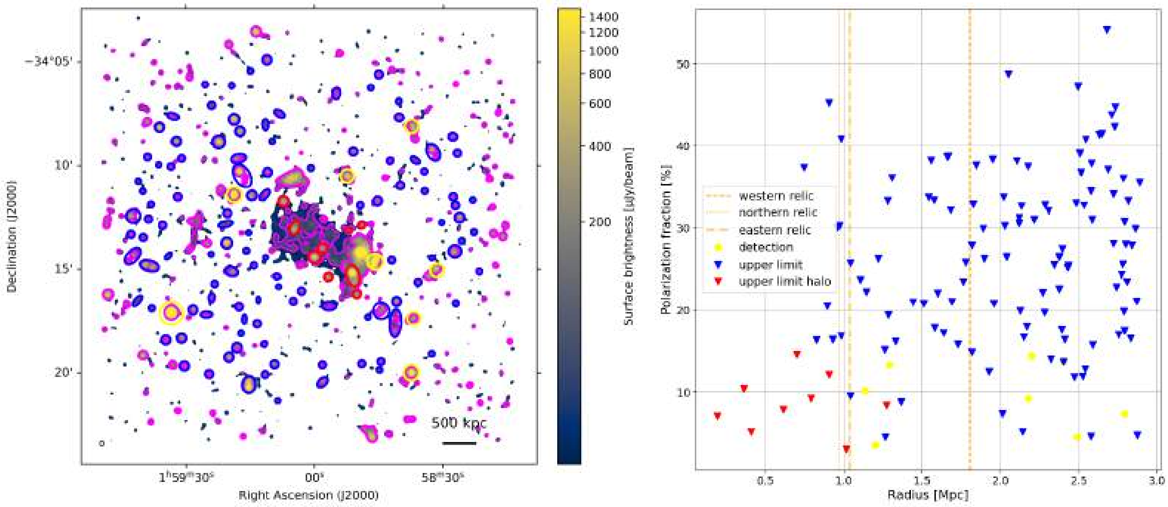

Figure 8.2: Left: same image shown in Fig.8.1 after discarding regions that were not large enough to cover a beam of the observation. Right: polarisation fraction profile of the regions present in the left panel. The orange vertical lines indicates the position of the relics.

The regions that survived the beam selection are shown in the left panel of Fig.8.2. This is the same image as in Fig.8.1, but only sources with extension larger than one beam are shown. The polarisation profile of the surviving regions is shown in the right panel. The yellow regions mark sources detected in polarisation (P), while the blue and red regions mark sources only detected in total intensity (I). Therefore, these regions are considered upper limit in P. The average P and I were computed over each source detected both in I and P. Upper limits were computed measuring the mean I and considering a 6 sigma upper limit for P. To compute the upper limit on P, the noise of the FDF spectrum in each pixel spectrum was considered.

Not all the regions selected as explained above could be used to construct the polarisation fraction profile. An additional selection was applied based on the intrinsic polarisation of the sources. Indeed, as radiosources are polarised at 10-15 % maximum at 1.4 GHz (e.g. Stil et al. (2014)) sources that have a low surface brightness would not appear polarised in our image due to their intrinsic polarisation, and not because of the depolarisation from the ICM. Hence, these sources are not useful to derive a limit on the cluster magnetic field. For this reason, upper limit regions with a polarisation fraction (P/I) exceeding the maximum measured P/I for regions with P detections were discarded.

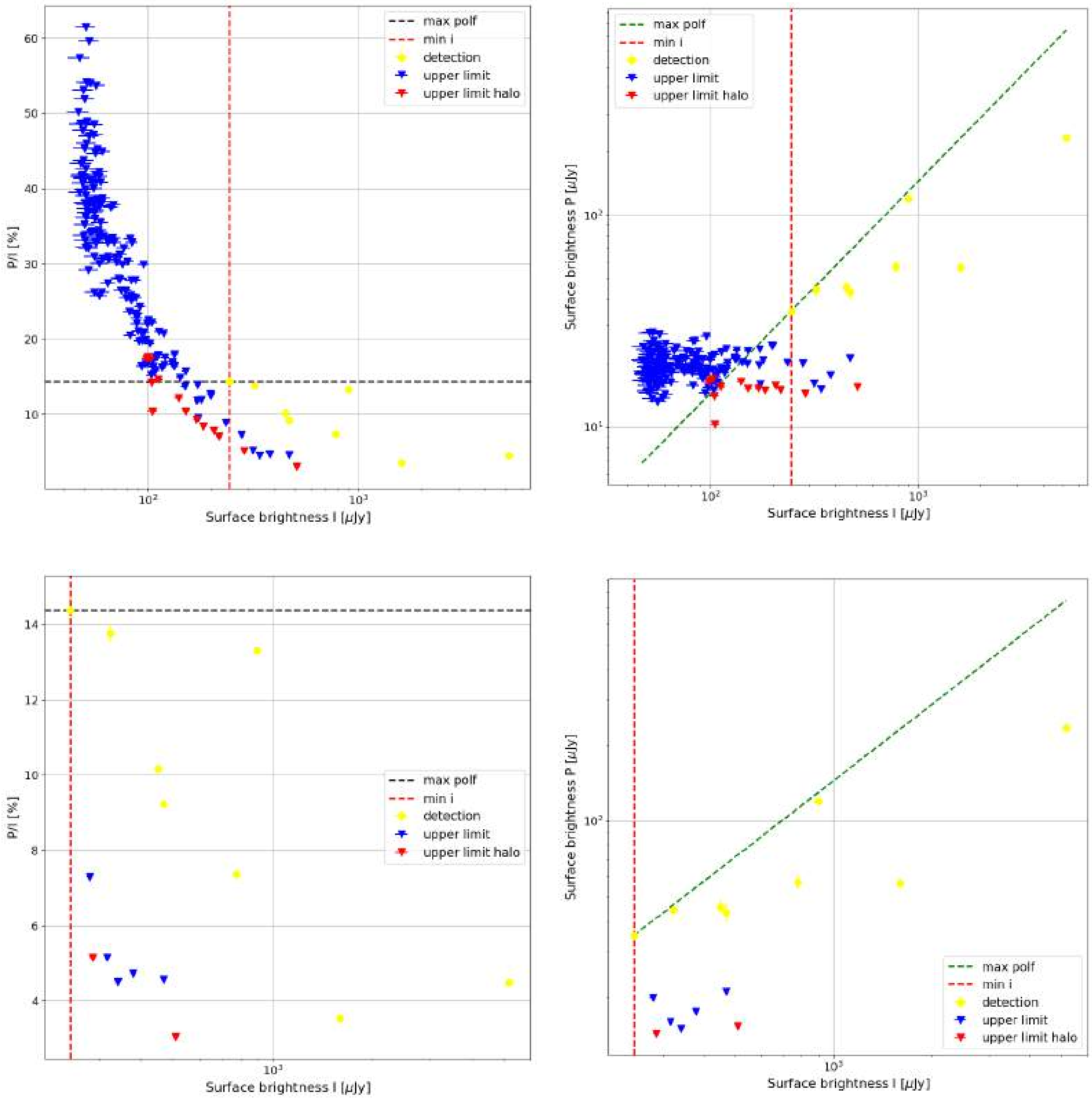

Figure 8.3: Top left panel: polarisation fraction vs total intensity (I) surface brightness, horizontal line at 14.4% and vertical line at 244 μJy/beam. Yellow points refers to regions with polarised intensity (P) emission while red and blue triangles refers to upper limit in P. Top right panel: polarised intensity (P) surface brightness vs total intensity (I) surface brightness. The green line indicates 14% and the red vertical line indicates the surface brightness of 244 μJy/beam. Same colors as before for the regions. Bottom panels: same as top ones but after the cut in maximum polarisation fraction.

Polarisation fraction vs total intensity (I) surface brightness and polarised intensity (P) surface brightness vs total intensity (I) surface brightness plots, before and after cut for maximum polarisation fraction measured, are shown in Fig.8.3. The lines are for the minimum total intensity (I) surface brightness 244 μJy/beam and maximum polarisation fraction measured 14%. Values of P/I exceeding the maximum measured polarisation were discarded.

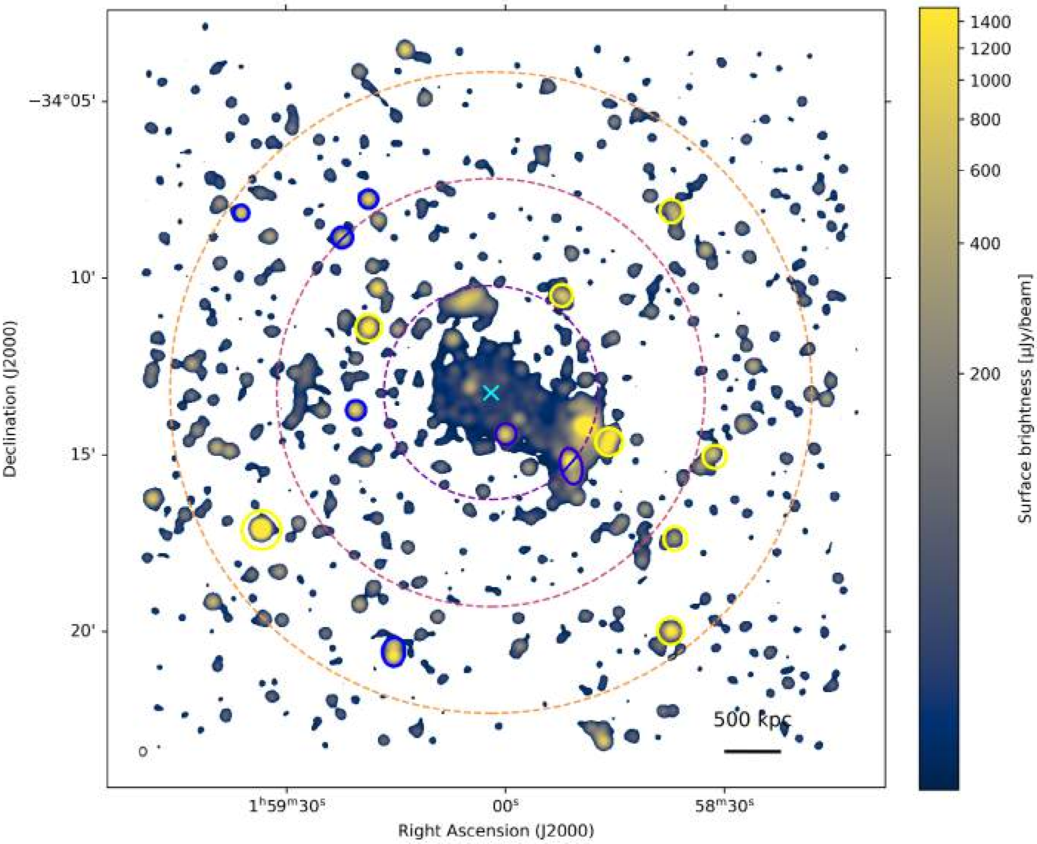

Figure 8.4: MeerKAT L-band total intensity (I) image of SZ2G243.15-73.84 after beam selection. Minor beam = major beam = 5.04″, noise ∼5.6 μJy/beam. Image masked at 5 times the noise. In blue the regions of total intensity emission in and out the radio halo, while in yellow, the regions of polarised intensity emission. Regions were discarded for maximum polarisation fraction. Radial annuli at 1, 2 and 3 Mpc. Image in Asinh scale.

The total intensity (I) image, with the remaining regions from beam selection and the cut for maximum polarisation fraction measured, is shown in Fig.8.4. In blue the regions of upper limit combining both regions in the radio halo and out. Radial annuli at 1, 2 and 3 Mpc define the annuli of extraction for the polarisation fraction profile, with center in RA = 01h 59m 02s and Dec = -34°13'16" (X-ray center). The positions of the sources were checked using **NED**[1] (NASA/IPAC Extragalactic Database) and all of them were found to lie in the background of the cluster. Some regions fell in between two different radial annuli, and an additional check on the beam was performed to ensure that each part of the region contained enough pixels to cover at least one beam of the observation.

---

[1] NED official website: `https://ned.ipac.caltech.edu/`

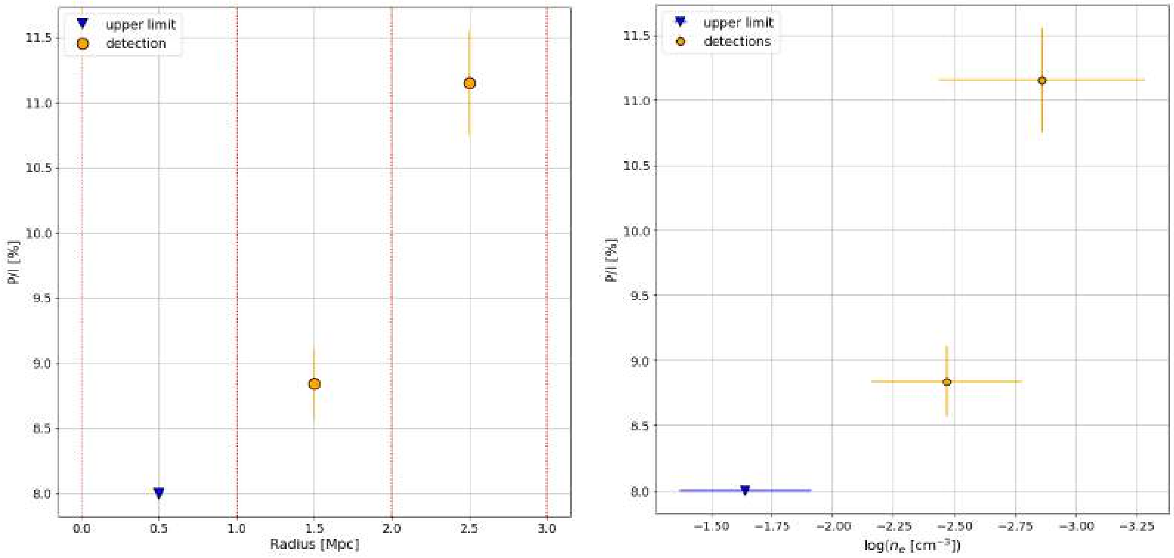

Figure 8.5: Left: polarisation fraction profile. Right: polarisation fraction profile with respect to density (density in log scale).

The polarisation fraction profile is shown in Fig.8.5. In the left panel as a function of the distance from the center and in the right as a function of the cluster density. The expected behavior of increasing polarisation fraction with radius and decreasing with density is seen in the figure. This is due to the higher density and magnetic field in the center of the cluster, leading to increased RM and RM dispersion (σ_{RM})(Osinga 2022 and Bonafede 2011). For the inner annulus, only upper limits were available, whereas measurements were present for the central and outer annulus.

8.3 Observed RM profile

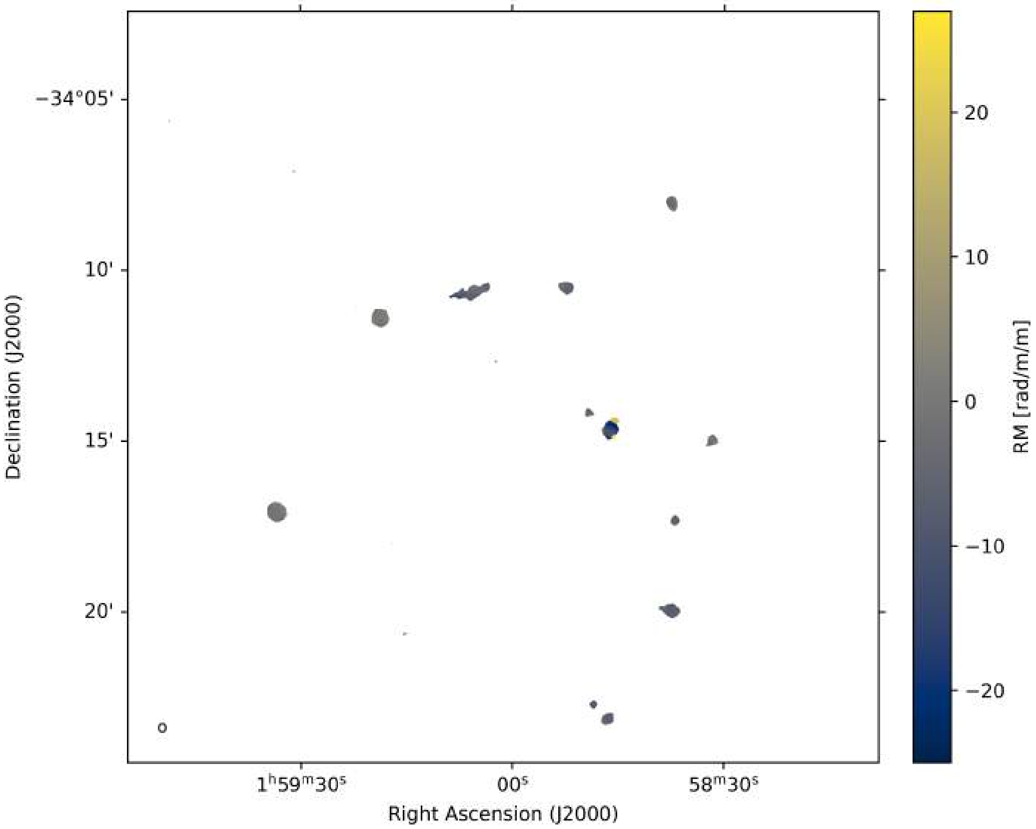

Figure 8.6: RM map masked at 5 times the total intensity I image, Fig.6.5, noise and 6 times the polarised intensity P noise of each pixel (as in right panel of Fig.6.8).

The RM map, produced using RM-synthesis and RM-clean (see Sec.6.2.7), is shown in Fig.8.6. The image is masked at five times the noise level of the total intensity I image (Fig.6.5), and for each pixel the peak of its FDF is required to exceed six times the spectrum noise, as in Sec.6.2.7. Very few pixels had signal in polarised intensity, therefore very few measurements of the RM were available. Hence, the idea of comparing the observed RM map with a simulated one was discarded.

8.4 Comparison with simulations

Using the MiRó code (see Sec.8.1 for a description of the code), a simulated RM map was generated from the density cube described at the end of Sec.7.2 and the magnetic field model (refer to Sec.8.1). The cube was created using the density profile derived from X-ray observations, including Gaussian scatter with a standard deviation equal to that of the X-ray surface brightness. The impact of using alternative density profiles is examined in Sec.8.5. The amplitude of the magnetic field used as a normalization in the code was computed with

$$B = B_{M'} \left(\frac{M}{M'}\right)^{b}, \tag{8.4.1}$$

where $B_{M'} = 2.11$ μG and b = 1.33. This resulted in a magnetic field of 3.7 μG, which for the code is the value of the mean magnetic field inside $R_{500} = 1.24$ Mpc. Eq.(8.4), with b = 1.33, was first derived in Dolag et al. (2002) through cosmological simulations, although $B_{M'}$ remained unconstrained. More recently, Balboni (2025b) obtained a value $B_{M'} = 2.11$ μG from observations of a sample of local galaxy clusters. The magnetic field is expected to scale with the gas density as in Eq.8.1.3. The parameter η, which links the strength of the magnetic field to the gas density, was set to 0.5 (Bonafede, 2010a). With this choice, the magnetic energy density scales in the same way as the thermal energy density.

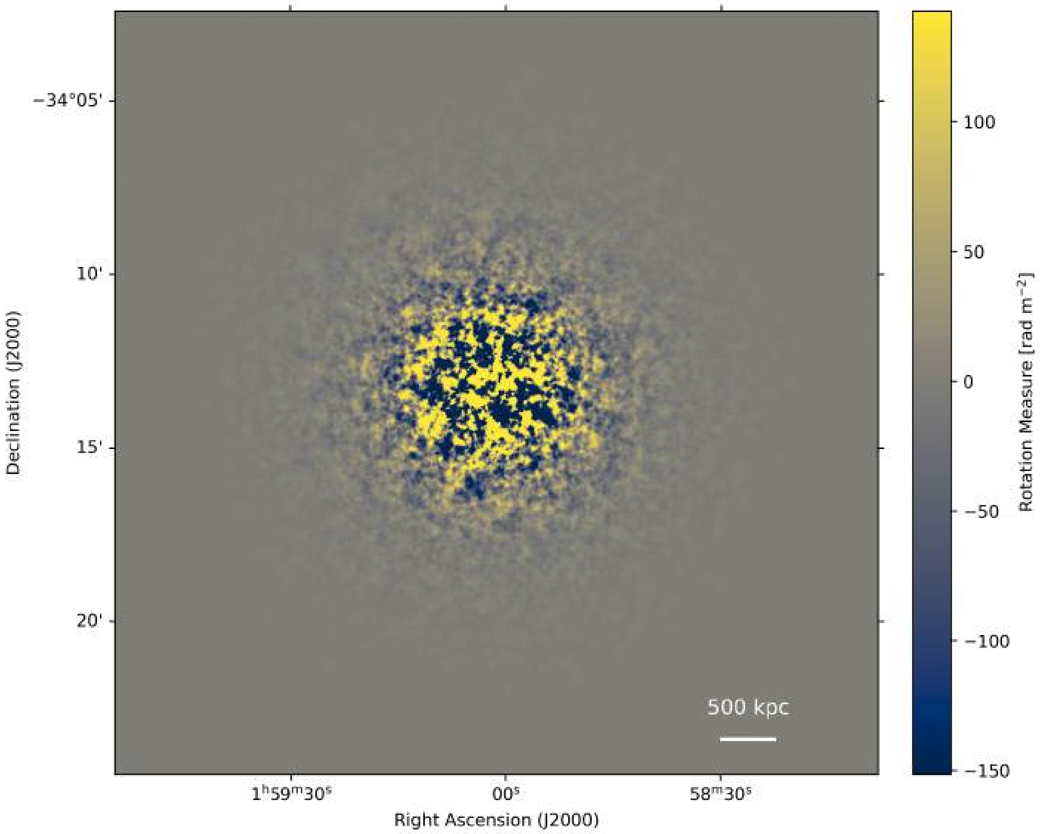

Figure 8.7: RM map simulated with the MiRó code. B normalization within R_{500} equal to 3.7 μG and $\eta = 0.5$.

The RM map obtained using the MiRó code is shown in Fig.8.7. As expected, the RM reaches higher values in the inner region, where the magnetic field is stronger and the density is higher. This RM map can be used to derive the effect of the beam depolarisation (refer to Sec.6.1.4), and create a polarisation fraction profile to compare with the observed one seen in Fig.8.5. If the simulated magnetic field matches the cluster magnetic field, a statistical agreement between the simulated and observed polarisation profiles is expected. This would suggest that Eq.8.4 correctly predicts the magnetic field also in clusters at $z > 0.4$. The simulated polarisation fraction profile was generated from a starting constant profile, set to the value of the outermost data point of the observed profile (Fig.8.5). The effect of beam depolarisation must be incorporated using the simulated RM map. To compute the depolarisation effect, an approach like the one used in De Rubeis (2024) was implemented. A uniform distribution of polarisation angle was assumed to cover the sky, $\chi_0 = 45°$. The chosen value is arbitrary and does not influence the outcome of the procedure, only its distribution has an effect. The assumption on the distribution was justified, since the sections of the RM map used had the same size as the regions corresponding to the polarised sources utilised to extract the observed polarisation fraction profile. This decision to not use the full RM map was made to closely replicate the procedure used to extract the observed polarisation fraction profile. Accordingly, the same regions shown in Fig.8.4 were used again to evaluate the depolarisation by beam and apply it to the simulated polarisation fraction profile. An intrinsic polarised intensity of $P_{intr} = 1$ Jy/beam was assumed for each pixel. The choice of $P_{intr} = 1$ Jy/beam is not relevant since the quantity of interest is the change in polarisation with beam size, P/P_{intr}, where P is the polarised intensity measured after convolving to the observational beam. The Faraday rotation was applied to the uniform angle distribution by using Eq.6.1.2

$$\chi = \chi_0 + \lambda^2 RM. \tag{8.4.2}$$

Stokes U and Q were derived from P_{intr} and χ using

$$Q = P_{intr} \cdot \cos(2\chi) \quad , \quad U = P_{intr} \cdot \sin(2\chi). \tag{8.4.3}$$

Stokes U and Q simulated images have been convolved to have the same beam of the observation, as in Sec.6.2.4. The convolved P was computed from Stokes U and Q by doing

$$P = \sqrt{U^2 + Q^2}, \tag{8.4.4}$$

and at this point the P/P_{intr} image was created. The loss of polarisation intensity due to beam depolarisation was derived in the following way

$$\frac{P}{P_{intr}} = \frac{P/I_{intr}}{P_{intr}/I_{intr}} = \frac{f_{pol,sim}}{f_{pol,intr}} \rightarrow f_{pol,sim} = \frac{P}{P_{intr}} \cdot f_{pol,intr}, \tag{8.4.5}$$

where f_{pol} is the polarisation fraction. Since the simulated polarisation fraction profile was constructed using the same regions and radial annuli as the observed one, a P/P_{intr} ratio was computed for each radial annulus. At large radii, the RM values become very low. As a consequence, two cases must be considered: the outermost data point may be affected by beam depolarisation, or it may not. In the former case, its value should be corrected for the depolarising effect. In the latter case, no correction is required because it already reflects the intrinsic polarisation (this assumption is explored in Sec.8.6). Since all the observed sources are located in the background of the cluster and the RM values in the simulation are low but not zero, the outermost point also had to be corrected for beam depolarisation. Therefore, the inverse of the outermost ratio was used to rescale the entire constant simulated polarisation fraction profile to the intrinsic polarisation level (recall that the simulated profile was initially set to a constant value equal to the outermost observed value). Each ratio was then applied to its corresponding radial annulus to account for beam depolarisation. The procedure to compute P/P_{intr} was repeated three additional times, each with the RM map rotated by 90°, so that the regions used to calculate the ratio sampled different parts of the map. In this way, multiple estimates of P/P_{intr} were obtained, allowing uncertainties to be assigned to the simulated polarisation fraction profile.

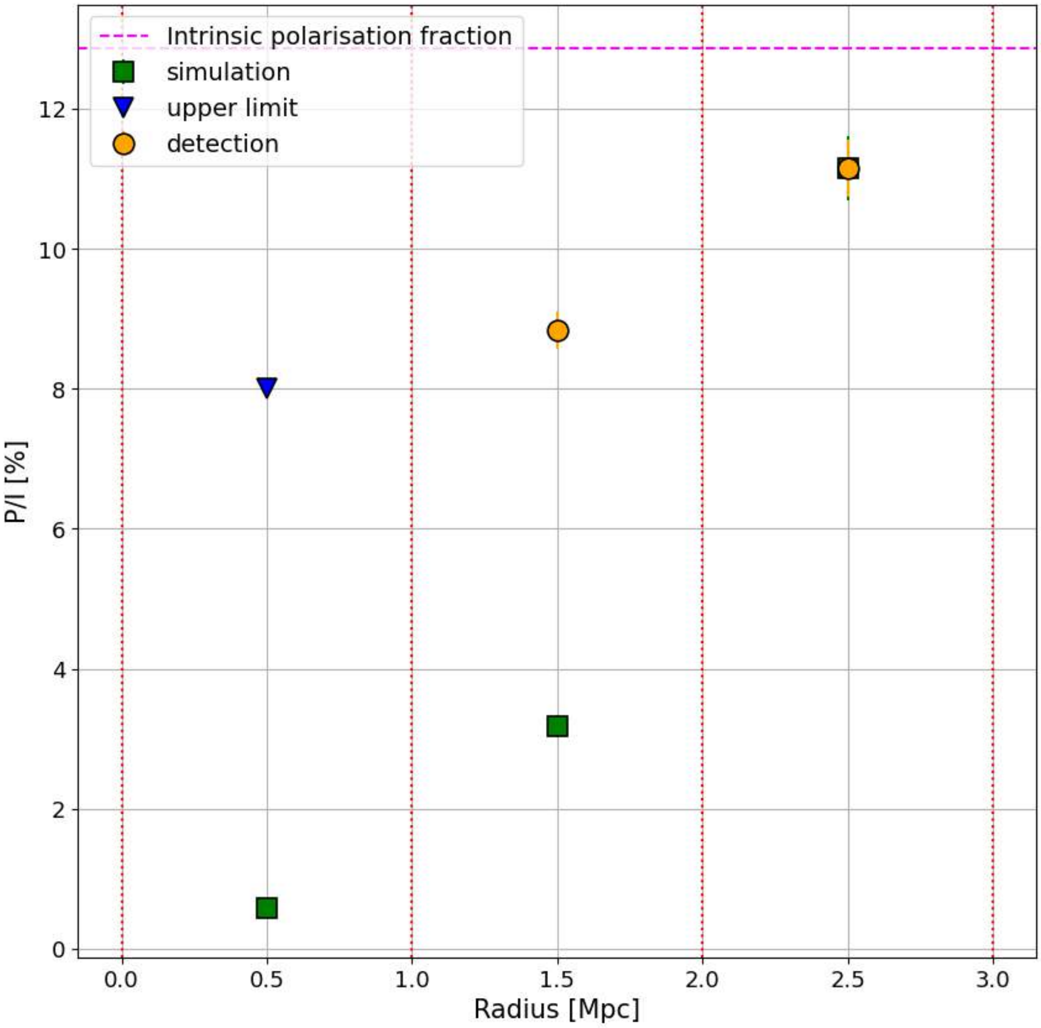

Figure 8.8: Comparison of observed and simulated polarisation fraction profile. The yellow and blue points are derived from observations, with the yellow points representing measured polarisation fractions and the blue point indicating an observational upper limit. The green points correspond to the simulated polarisation fraction profile. The magenta horizontal line indicates the intrinsic polarisation fraction.

The comparison between the simulated and observed polarisation fraction profile is shown in Fig.8.8. Observational data are shown in yellow and blue, where yellow indicates measured polarisation fractions and blue represents an observational upper limit. The simulated polarisation fraction profile is displayed in green. The magenta horizontal line indicates the intrinsic polarisation fraction. The outermost point was used as an anchor between the two profiles, resulting in the observed and simulated values coinciding. The innermost simulated point lies below the observed upper limit. The central simulated point is significantly more depolarised compared to the observations. This is due to a larger variation of the RM within the beam (σ_{RM}) in the simulated RM map compared to the actual physical counterpart. Assuming the gas density is well constrained from X-ray observations, the additional depolarising effect caused by σ_{RM} depends solely on the magnetic field. Hence, Eq.8.4 predicted a magnetic field strength too high to reproduce the value derived from the observation.

Since the $B-M$ relation was fitted using clusters at $z < 0.4$ Balboni (2025b), this discrepancy suggested that PSZ2G243.15-73.84, lying at $z = 0.41$, does not follow the behavior observed in the local cluster sample. An approximate estimate of the magnetic field needed for the simulated and observed profiles to match was obtained by scaling the predicted value, $B = 3.7$ μG, by the ratio between the simulated and observed polarisation fractions at the central point of the profile. This approach assumed that the full contribution to σ_{RM} arose from the magnetic field. The resulting value, $B = 1.3$ μG, is about 3 times lower than the predicted 3.7 μG. Additional simulations would be needed to test this lower magnetic field, but this is beyond the scope of this thesis and will be investigated in the future.

Eq.8.4 depends on three parameters: the cluster mass M, b, and $B_{M'}$. A lower limit for the predicted magnetic field can be estimated by using the lower bounds of these parameters. The lower bound for the mass of PSZ2G243.15-73.84 is given in Balboni (2025a), $M_{500} = (8.09 - 0.49) \times 10^{14} M_{\odot}$. The lower bound for $B_{M'}$ is given in Balboni (2025b), $B_{M'} = 2.11 - 0.88$ μG. No lower limit was considered for b. Using these bounds, the resulting lower limit for B was 2.0 μG, which remained above 1.3 μG and was therefore insufficient to reconcile the profiles. Consequently, this strengthens the claim that PSZ2G243.15-73.84 behaves differently from local clusters, by not following Eq.8.4.

In Balboni (2025b) two sets of best-fit parameters for the $B - M$ relation were obtained: $b = 1.33$ & $B_{M'} = 2.11$ μG, which have been used in the analysis so far, and $b = 2.05$ & $B_{M'} = 2.52$ μG. Using the second set, Eq.8.4 predicts a significantly stronger magnetic field, ~ 6 μG, nearly twice the value of 3.7 μG. This would induce even more beam depolarisation in the simulated polarisation profile; therefore, this set was discarded as a plausible option.

8.5 Impact of the gas model on the simulated polarisation profile

The results obtained in the previous section depend on the gas density of the cluster. The gas density was modeled as explained in Chap.7 taking into account the scatter. In this section, the impact of two scenarios is investigated: neglecting the scatter in the density profile and using the universal density profile for clusters as presented in Ghirardini (2019).

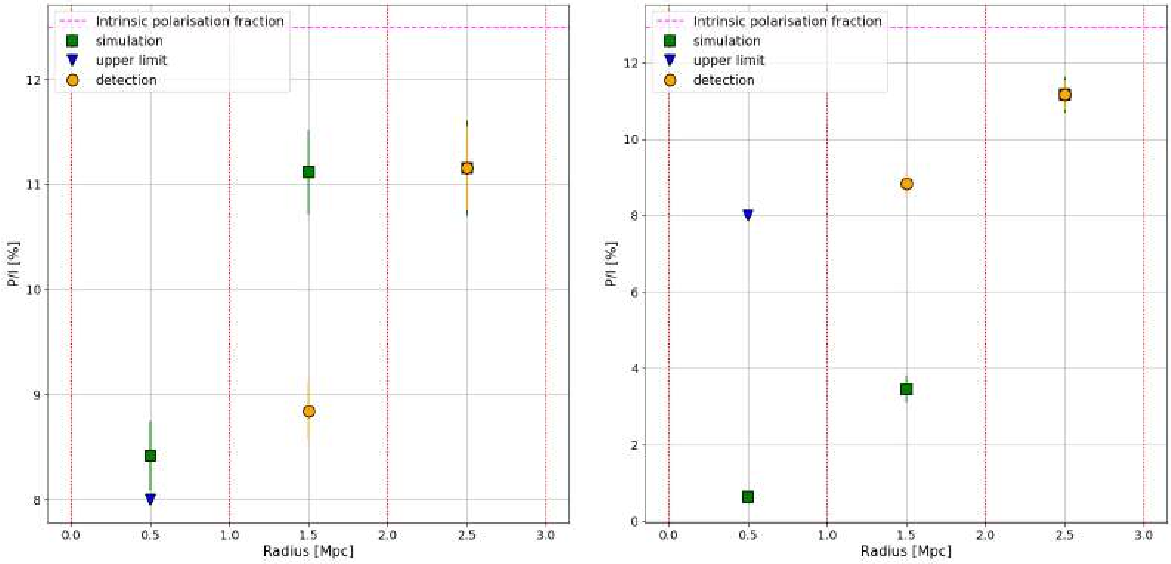

Figure 8.9: Comparisons of observed and simulated polarisation fraction profile (as in Fig.8.8). The simulated polarisation fraction profiles were generated using different RM maps produced by the MiRó code, using as input density profiles other than the one used for the profiles presented in Sec.8.4. Left panel: the input density profile was the universal (analytical) profile for galaxy clusters described in Ghirardini (2019). Right panel: the input density profile was the same used in Sec.8.4 and shown in Fig.7.4, but without the addition of scatter.

The simulated polarization fraction profile shown in the right panel of Fig.8.9 was produced assuming that the gas density profile derived from X-ray observations had no scatter. No substantial difference was observed compared to the case shown in Fig.8.8. Adding or omitting a Gaussian scatter in the density did not produce a meaningful change, except for a slight increase in the uncertainty, which is most noticeable in the central simulated data point, where the polarization fraction was 3.2% with scatter and 3.5% without.

Utilizing the universal density profile (Ghirardini, 2019) as input for the MiRó code led to a different simulated polarisation fraction profile, shown in the left panel of Fig.8.9. In this case the magnetic field strength was insufficient to depolarise the simulated point below the observed upper limit. Therefore, a stronger magnetic field would have been needed to reproduce the observed polarisation fraction profile. This result is opposite to what was suggested by the comparison of the polarisation fraction profiles in Fig.8.8 and in the right panel of Fig.8.9 (also in Fig.8.10 of Sec.8.6). The difference between the simulated polarization fraction profile derived from the universal density profile and that obtained from X-ray observations of PSZ2G243.15-73.84 highlights that in studies of this type, care must be taken when using universal gas density profiles, as relying on them without cluster-specific measurements can lead to misleading conclusions.

8.6 Different assumption for the intrinsic polarisation

In Sec.8.4, it was assumed that the outermost data point was affected by beam depolarisation, even though it lies far from the cluster center where the RM values are low. Here, an alternative scenario is considered, in which the same simulated profile in Sec.8.4 is used but the outermost data point is assumed to be unaffected by beam depolarisation, and thus directly represents the intrinsic polarisation fraction. Although this scenario is less plausible than the one adopted in Sec.8.4, it is included for the sake of completeness.

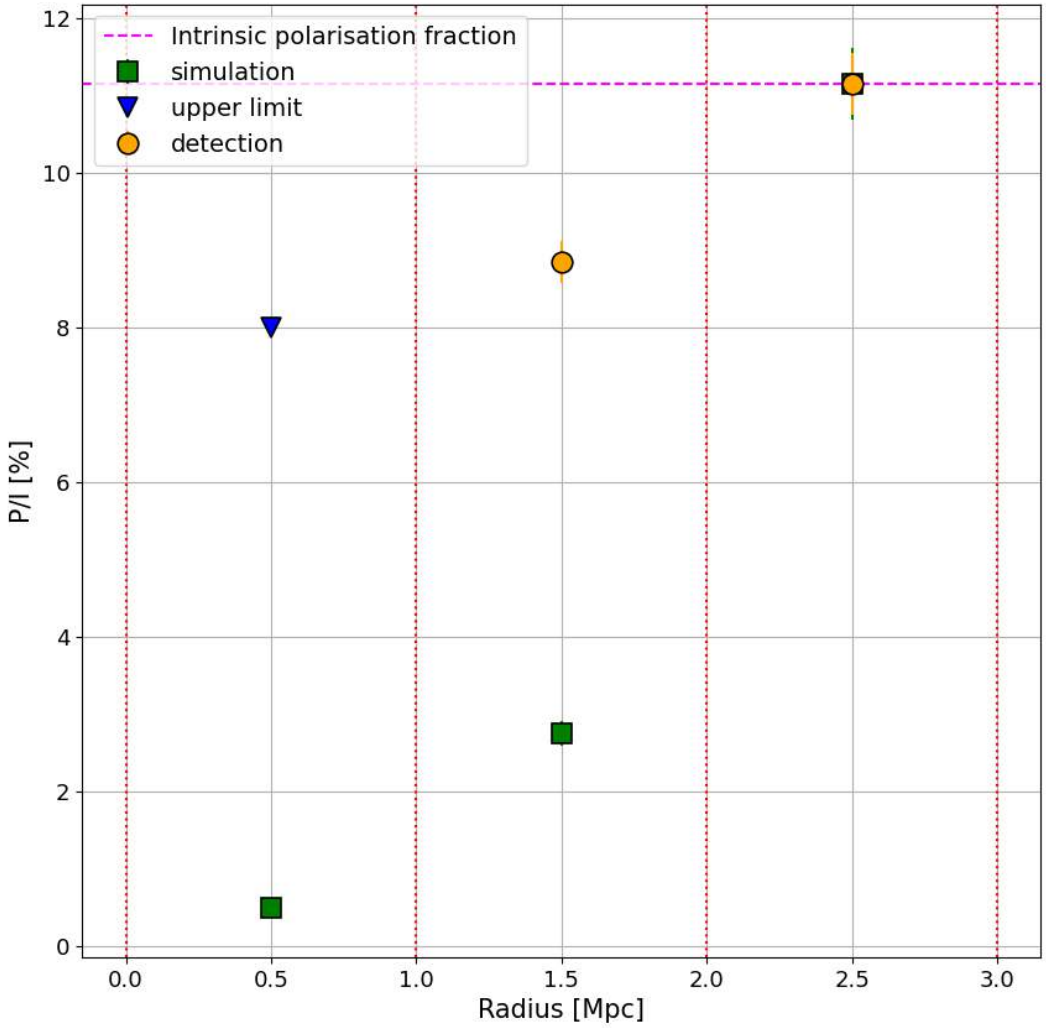

Figure 8.10: Comparison of observed and simulated polarisation fraction profiles (as in Fig.8.8). Contrary to Sec.8.4, the outermost point is assumed not to be affected by beam depolarisation.

The comparison between simulated and observed profiles is shown in Fig.8.10. Assuming intrinsic polarization for the outermost point resulted in a shift of the entire simulated polarization fraction profile, yet no agreement with the observed profile was achieved. The simulated profile showed no improvement and the discrepancy with the observed polarization fraction profile persisted.

The assumption of no beam depolarisation for the outermost data point is considerably stronger and far less likely than the assumption made in Sec.8.4, where this point was considered depolarised despite being located far from the cluster center. This is supported by the simulated *RM* maps (Fig.8.7), which show values of few tens of rad/m^2 at 2-3 Mpc from the cluster center (corresponding to the annuli of the outermost point). Moreover, the observed *RM* map (Fig.8.6) exhibits the same behavior.

From this analysis, it was concluded that the magnetic field predicted by Eq.8.4 is overestimated, regardless of the assumption made about the intrinsic polarization.

Chapter 9

Final discussion

9.1 Results

- In this work, MeerKAT radio polarisation observations were analyzed with the aim of inferring the strength of the magnetic field in PSZ2G243.15-73.84 and assessing whether the prediction linking magnetic field and cluster mass, Eq.8.4 ($B-M$ relation) as discussed in Dolag et al. (2002) and Balboni (2025b), correctly describes the magnetic field of this galaxy cluster. The goal was to extract a radial polarisation fraction profile and a RM map from the radio observations, and compare them with simulated versions generated using the MiRó code and based on the $B-M$ relation prediction.

- The MeerKAT data were already calibrated. However, self calibration was performed, resulting in improved image quality, with lower noise and weaker artifacts.

- The total intensity (I) image and the Stokes Q and U images were generated with the aim of performing RM-synthesis to correct for bandwidth depolarisation. To achieve this, the Stokes Q and U images were divided into 186 channels to account for the range of RM values expected in galaxy clusters, typically a few hundred rad/m^2 and up to about 1000 rad/m^2 in the centers of massive cool core clusters.

- Channels were selected based on the beam and noise of the images. If either of these was too high according to the criteria specified in Sec.6.2, the channel was discarded, and the remaining ones were convolved to a common beam of $11.4''$ (62.8 kpc).

- RM-synthesis (and RM-clean) produced a FDF spectrum for each pixel. Most pixels did not contain any polarised signal, and the remaining ones exhibited simple spectra with one prominent peak at low RM values. This was true even for the pixels belonging to the relics. This indicates that internal depolarisation in the extended sources of the cluster, namely the halo, was too strong to produce sufficient polarised signal to recover a complex FDF spectrum. The same behavior has been observed in other radio halos (Bonafede, 2010b).

- From the FDF spectra, a linearly polarised intensity (P) image, an RM map shown in Fig.8.6 and a polarisation fraction image shown in the right panel of Fig.6.8 were created. The polarisation fraction image also shows the polarisation vectors corrected for RM, taking into account also the contribution from the Milky Way RM. Very few pixels contained significant P signal, resulting in a sparsely populated RM map. Therefore, the approach of comparing the observed and simulated RM maps was discarded.

- The MiRó code requires a density cube as input in order to produce a simulated RM map. For this reason, the density profile was obtained by deprojecting the surface-brightness profile, extracted from the X-ray observations. When constructing the cube, a scatter proportional to the standard deviation of the surface brightness was added to the density, although reduced in amplitude to avoid the appearance of unphysical negative values. This is the first time that scatter in the density profile has been included in a study of this kind. Previous works have always relied on "smooth" (without scatter) density profiles.

- The radial profile of the polarisation fraction was extracted from the polarisation fraction map obtained through the RM-synthesis results. The regions used for the extraction were identified using the contour levels corresponding to 9 and 18 times the noise of the total intensity (I) image (refer to Fig.8.1). Regions too small to cover at least one synthesized beam, as well as upper limit regions (detection in I but not P) whose polarisation fraction falls below the lowest value measured in the P detection regions, were discarded. The retrieved polarisation fraction profile consisted of three points and extended out to 3 Mpc, with radial annuli of 1 Mpc each. The innermost point was an upper limit, while the other two were detections. The fractional polarisation profile (Fig.8.5) showed an increase with radius (left panel) and a decrease with gas density (right panel). At larger radii, the lower density leads to smaller values of RM and σ_{RM}, reducing the impact of the depolarisation.

- The MiRó code required as input a density cube and a magnetic field cube to generate a simulated RM map. The density cube was the one constructed using the density profile derived from X-ray observations. The magnetic field cube was generated by the code itself, assuming random phases, Gaussian components, a power spectrum as described in Domínguez-Fernández (2019), magnetic energy density scaling in the same way as the thermal energy density (Bonafede, 2010a), and a mean magnetic field within R_{500} of $B = 3.7$ μG, as predicted by the $B - M$ relation described in Dolag et al. (2002) and Balboni (2025b). The resulting RM map (Fig.8.7) was used to estimate the beam depolarisation, which was then utilized to create a simulated polarisation fraction profile. This profile was generated starting from the outermost point of the observed polarisation fraction profile, under the assumption that it was affected by beam depolarisation even if positioned very far from the cluster center. The comparison between the observed and simulated profiles showed no agreement (Fig.8.8). The depolarisation of the simulated polarisation fraction profile was stronger than that of the observed profile, indicating that the magnetic field used in the simulation, $B = 3.7$ μG, was too high.

- An approximate estimate of the magnetic field required to match the simulated and observed polarisation fraction profiles yielded a value of 1.3 μG. Considering the lower limit of the parameters used in Eq.8.4, a lower limit for the predicted magnetic field was found to be 2 μG. This lower limit was nearly twice the value needed for the profiles to match, thereby reinforcing the claim that PSZ2G243.15-73.84 behaves differently from local clusters, not following Eq.(8.4).

- Considering a density cube based on the same density profile previously used, but without scatter, resulted in a slightly lower depolarisation and bigger uncertainty. Instead, using the density profile described in Ghirardini (2019) produced a completely different result: the magnetic field is not strong enough to depolarise the simulated point below the observed upper limit. This highlighted that in studies of this type, care must be taken when using universal gas density profiles. Then, it was investigated an alternative scenario, assuming that the outermost point is not affected by beam depolarisation. In this case, the simulated polarisation fraction profile obtained using the gas density profile from observations resulted again too low with respect to observations.

- In Balboni (2025b) other values for the parameters of Eq.8.4 are discussed; however, using them would predict an even stronger magnetic field, resulting in greater depolarisation in the simulated polarisation fraction profile and thereby increasing the discrepancy with the observed profile.

- Eq.8.4 overestimated the magnetic field strength in PSZ2G243.15-73.84, producing a simulated polarisation fraction profile with depolarisation that was too strong compared to the observations. This discrepancy highlighted that the magnetic field in this high redshift cluster ($z = 0.41$, meaning not local universe) did not follow the trend observed in nearby systems, for which Eq.8.4 successfully predicts the behavior (Dolag et al., 2002; Balboni, 2025b). Such a conclusion contrasted with the general expectation that high z galaxy clusters should host magnetic fields comparable to those in local clusters. Di Gennaro (2021) found that the high radio luminosities of distant clusters indicated magnetic field strengths comparable to those in nearby systems. Our study, instead, indicates a lower magnetic field with respect to local clusters, which would alleviate the problem of fast amplification raised by Di Gennaro (2021). However, more clusters at high redshift ($z > 0.4$) should be investigated to better address this issue.

Appendix A

Parameters

A.1 WSClean

WSClean parameters used for imaging

1. **minuv-l**: set minimum (u, v) values to be gridded.
2. **size**: image size in pixels.
3. **reorder**: reorganization of the data to simplify their handling by the software.
4. **weight**: robustness parameter to select the desired level between uniform and natural weighting.
5. **parallel-reordering**: enable parallel reordering.
6. **mgain**: sets the major iteration gain, during every major iteration, the peak is reduced by this factor.
7. **data-column**: select data to use.
8. **join-channels**: enable multi-frequency deconvolution, peak finding is performed in the sum of all channels.
9. **channels-out**: number of batches of channels.
10. **parallel-deconvolution**: separately deconvolve the sub-images.
11. **parallel-gridding**: enable parallel gridding.
12. **auto-mask**: clean until chosen sigma level, while creating a mask.
13. **auto-threshold**: clean until chosen sigma level inside the mask created with **auto-mask**.
14. **fits-mask**: use external mask.
15. **save-source-list**: save component list.
16. **fit-spectral-pol**: enforces spectral smoothness by fitting a polynomial to the brightness across channels.

17. **pol**: select polarisation.
18. **gridder**: select gridder algorithm.
19. **wgridder-accuracy**: maximum acceptable RMS error of the wgridder result when compared to a direct Fourier transform.
20. **scale**: angular size of a single pixel.
21. **nmiter**: maximum number of major iterations.
22. **niter**: maximum number of minor iterations.
23. **abs-threshold**: noise threshold for minor iterations.
24. **multiscale**: enable multiscale deconvolution.
25. **multiscale-scales**: select scales that are to be used in multiscale.
26. **join-polarisations**: peak finding is searched over the squared sum of polarisation intensities.
27. **join-channels**: Peak finding is performed in the sum over channels.

A.2 facetselfcal

facetselfcal parameters used for self calibration

1. **soltype-list**: list with solution types (other lists stick to the same order defined here).
2. **solint-list**: solution interval corresponding to solution types.
3. **nchan-list**: number of channels corresponding to solution types.
4. **smoothnessconstraint-list**: list with frequency smoothness values in MHz.
5. **noarchive**: do not archive the data.
6. **uvminim**: inner *uv*-cut for imaging in lambda.
7. **imsize**: image size.
8. **pixelsize**: pixels size in arcsec.
9. **beamcor**: correct the visibilities for beam in the phase center.
10. **channelsout**: number of channels out during imaging (as for **WSCleann**).
11. **niter**: number of iterations (as for **WSClean**).
12. **paralleldeconvolution**: parallel-deconvolution size for **WSClean**.
13. **start**: start selfcal cycle at this iteration number.
14. **stop**: stop selfcal cycle at this iteration number.

15. **multiscale**: use multiscale deconvolution (as for **WSClean**).
16. **multiscale-start**: start multiscale deconvolution at this selfcal cycle.
17. **doflagging**: flag on complexgain solutions via RMS outlier detection.
18. **useaoflagger**: run AOflagger on input data.
19. **aoflagger-strategy**: use this strategy for AOflagger.
20. **clipsolhigh**: flag amplitude solutions above this value.
21. **clipsollow**: flag amplitude solutions below this value.
22. **clipsolutions**: flag amplitude solutions above **clipsolhigh** and below **clipsollow**.
23. **parallelgridding**: parallel-gridding for **WSClean**.
24. **remove-outside-center**: subtract sources that are outside the central parts of the FoV. In case you want something else set –**remove-outside-center-box**.
25. **remove-outside-center-box**: user defined box **DS9** region file to subtract sources that are outside this part of the image.

Appendix B

Commands

B.1 WSClean

WSClean command used to generate the image shown in fig.(3.2)

```
-minuv-l 10.0 -size 11000 11000 -reorder -weight briggs -0.5
-parallel-reordering 4 -mgain 0.8 -data-column DATA -join-channels
-channels-out 12 -parallel-deconvolution 1024 -parallel-gridding 4 -auto-mask 2.5
-auto-threshold 0.5 -save-source-list -fit-spectral-pol 3 -pol i -gridder wgridder
-wgridder-accuracy 0.0001 -scale 1.2arcsec -nmiter 12 -niter 50000
```

WSClean command used to generate the image shown in fig.(5.1)

```
-minuv-l 10.0 -size 1100 1100 -reorder -weight briggs -0.5 -multiscale
-multiscale-scales 0,4,8,16,32,64,128 -parallel-reordering 4 -mgain 0.8
-data-column DATA -join-channels -channels-out 12 -parallel-deconvolution 1024
-parallel-gridding 4 -auto-mask 2.5 -auto-threshold 0.5 -save-source-list
-fit-spectral-pol 3 -pol i -gridder wgridder -wgridder-accuracy 0.0001
-scale 1.2arcsec -nmiter 12 -niter 50000
```

WSClean command used to generate the image shown in fig.(5.2)

```
-minuv-l 10.0 -size 1100 1100 -reorder -pol QU -join-polarisations -join-channels
-channels-out 186 -weight briggs -0.5 -parallel-reordering 4 -mgain 0.8
-data-column DATA -parallel-deconvolution 1024 -parallel-gridding 4
-abs-threshold 0.847e-6 -fits-mask pol_mask_defaultbox_multiscale_I
-gridder wgridder -wgridder-accuracy 0.0001 -scale 1.2arcsec -nmiter 12
-niter 5000000
```

B.2 facetselfcal

facetselfcal commands used to generate the images shown in fig.(4.2) (except the one in the bottom right panel) The first 4 rounds were only about the phase.

```
--soltype-list="[’scalarphase’]" --solint-list="[’2min’]"
--nchan-list=[1] --soltypecycles-list=[0] --smoothnessconstraint-list="[100.]"
--noarchive --uvminim=10 --imsize=11000 --pixelsize=1.2 --beamcor=no
--channelsout=12 --niter=50000 --paralleldeconvolution=1024 --start=0 --stop=4
--multiscale--doflagging=False --useaoflagger
--aoflagger-strategy="default_StokesV.lua" --clipsolutions --multiscale-start=0
--parallelgridding=4
```

Then 3 rounds of both phase and amplitude.

```
--soltype-list="['scalarcomplexgain']" --solint-list="['5min']"
--nchan-list=[1] --soltypecycles-list=[0] --smoothnessconstraint-list="[100.]"
--noarchive --uvminim=10 --imsize=11000 --pixelsize=1.2 --beamcor=no
--channelsout=12 --niter=50000 --paralleldeconvolution=1024 --start=0 --stop=4
--multiscale--doflagging=False --useaoflagger
--aoflagger-strategy="default_StokesV.lua" --clipsolutions --multiscale-start=0
--parallelgridding=4
```

A final round of both phase and amplitude.

```
--soltype-list="['scalarcomplexgain']" --solint-list="['5min']"
--nchan-list=[1] --soltypecycles-list=[0] --smoothnessconstraint-list="[100.]"
--noarchive --uvminim=10 --imsize=11000 --pixelsize=1.2 --beamcor=no
--channelsout=12 --niter=50000 --paralleldeconvolution=1024 --start=0 --stop=4
--multiscale--doflagging=False --useaoflagger
--aoflagger-strategy="default_StokesV.lua" --clipsolutions --multiscale-start=0
--parallelgridding=4 --remove-outside-center
--remove-outside-center-box="cluster_size.reg"
```

Bibliography

Arnaud, M. (2020). The cluster heritage project with xmm-newton: Mass assembly and thermodynamics at the endpoint of structure formation. i. programme overview. *arXiv e-prints*.

Balboni, M. (2025a). Chex-mate: New detections and properties of the radio diffuse emission in massive clusters with meerkat. *arXiv e-prints*.

Balboni, M. (2025b). Chex-mate: Scaling relations of radio halo profiles for clusters in the lotss dr2 area. *Astronomy & Astrophysics*, 695.

Bartalucci, I. (2023). Chex-mate: Constraining the origin of the scatter in galaxy cluster radial x-ray surface brightness profiles. *Astronomy & Astrophysics*, 674.

Bonafede, A. (2010a). The coma cluster magnetic field from faraday rotation measures. *Astronomy & Astrophysics*, 513.

Bonafede, A. (2010b). Galaxy cluster magnetic fields from radio polarized emission. *PoS ISKAF2010*.

Bonafede, A. (2011). Fractional polarization as a probe of magnetic fields in the intra-cluster medium. *Astronomy & Astrophysics*, 530.

Bonafede, A. (2013). Measurements and simulation of faraday rotation across the coma radio relic. *Monthly Notices of the Royal Astronomical Society*, 433:3208–3226.

Brentjens, M. A. and de Bruyn, A. G. (2005). Faraday rotation measure synthesis. *Astronomy & Astrophysics*, 441:1217–1228.

Burn, B. J. (1966). On the depolarization of discrete radio sources by faraday dispersion. *Monthly Notices of the Royal Astronomical Society*, 133.

CASA tutorial (2021). *CASA imsmooth Tutorial-CASA5.7.0.*

Condon, J. J. and Ransom, S. M. (2016). *Essential Radio Astronomy.* Princeton University Press.

De Rubeis, E. (2024). Magnetic fields in the outskirts of psz2 g096.88+24.18 from depolarization analysis of radio relics. *arXiv e-prints*.

Di Gennaro, G. (2021). Fast magnetic field amplification in distant galaxy clusters. *Nature Astronomy*, 5:268–275.

Dolag, K., Bartelmann, M., and Lesch, H. (2002). Evolution and structure of magnetic fields in simulated galaxy clusters. *Astronomy & Astrophysics*, 387:383–395.

Domínguez-Fernández, P. (2019). Dynamical evolution of magnetic fields in the intracluster medium. *Monthly Notices of the Royal Astronomical Society*, 486:623–638.

Eckert, D. (2016). The xxl survey xiii: Baryon content of the bright cluster sample. *Astronomy & Astrophysics*, 592.

Eckert, D. (2020). Low-scatter galaxy cluster mass proxies for the erosita all-sky survey. *Open Journal of Astrophysics*, 3.

Ettori, S. (2010). From "universal" profiles to "universal" scaling laws in x-ray galaxy clusters. *arXiv e-prints*.

Feretti, L. (2012). Clusters of galaxies: observational properties of the diffuse radio emission. *Astronomy and Astrophysics Review*, 20.

Gan, H. and Mertens, F. G. (2023). Assessing the impact of two independent direction-dependent calibration algorithms on the lofar 21-cm signal power spectrum. *Astronomy & Astrophysics*, 669.

George, S. J. (2013). Detection thresholds and bias correction in polarized intensity. *Publications of the Astronomical Society of Australia*.

Ghirardini, V. (2019). Universal thermodynamic properties of the intracluster medium over two decades in radius in the X-COP sample. *A&A*, 621:A41.

Hales, C. A. (2012). Analytic detection thresholds for measurements of linearly polarized intensity using rotation measure synthesis. *Monthly Notices of the Royal Astronomical Society*, 424:2160–2172.

Heald, G. (2009). The faraday rotation measure synthesis technique. In *IAU Symposium 259, Cosmic Magnetic Fields: From Planets, to Stars and Galaxies*, pages 591–602.

Hudson, D. S. (2010). What is a cool-core cluster? a detailed analysis of the cores of the x-ray flux-limited hiflugcs cluster sample. *Astronomy & Astrophysics*, 513.

Murgia, M. (2004). Magnetic fields and faraday rotation in clusters of galaxies. *arXiv e-prints*.

Offringa, A. R., McKinley, B., Hurley-Walker, et al. (2014). WSClean: an implementation of a fast, generic wide-field imager for radio astronomy. *MNRAS*, 444(1):606–619.

Offringa, A. R. and Smirnov, O. (2017). An optimized algorithm for multi-scale wide-band deconvolution of radio astronomical images. *arXiv e-prints*.

Osinga, E. (2022). The detection of cluster magnetic fields via radio source depolarisation. *Astronomy & Astrophysics*, 665.

Purcell, C. R. (2020). Rm-tools: Rotation measure (rm) synthesis and stokes qu-fitting. `https://ui.adsabs.harvard.edu/abs/2020ascl.soft05003P/abstract`. Astrophysics Source Code Library.

Rasia, E. (2013). X-ray morphological estimators for galaxy clusters. *arXiv e-prints*.

Riseley, C. J. (2022). A meerkat-meets-lofar study of ms 1455.0+2232: A 590 kpc “mini”-halo in a sloshing cool-core cluster. *Monthly Notices of the Royal Astronomical Society*, 512(3):4210–4230.

Rossetti, M. (2024). Chex-mate: Robust reconstruction of temperature profiles in galaxy clusters with xmm-newton. *arXiv e-prints*.

Rybicki, G. B. and Lightman, A. P. (2004). *Radiative Processes in Astrophysics*. Wiley-VCH.

Sanderson, R., O’Sullivan, E., and Ponman, T. (2009). A statistically selected chandra sample of 20 galaxy clusters – ii. gas properties and cool core/non-cool core bimodality. *Monthly Notices of the Royal Astronomical Society*, 395:764–776.

Schwab, F. R. (1984). Relaxing the isoplanatism assumption in self-calibration; applications to low-frequency radio interferometry. *AJ*, 89:1076–1081.

Shneider, C. (2014). Depolarization of synchrotron radiation in a multilayer magneto-ionic medium. *Astronomy & Astrophysics*, 567.

Smith, R. K. (2001). Collisional plasma models with apec/aped: Emission-line diagnostics of hydrogen-like and helium-like ions. *The Astrophysical Journal*, 556.

Stil, J. M., Keller, B. W., George, S. J., and Taylor, A. R. (2014). Degree of polarization and source counts of faint radio sources from stacking polarized intensity. *Astrophysical Journal*, 787(2):99.

Stokes, G. G. (1851). On the composition and resolution of streams of polarized light from different sources. *Transactions of the Cambridge Philosophical Society*, 9:399.

Stuardi, C. (2021). The intra-cluster magnetic field in the double relic galaxy cluster abell 2345. *arXiv e-prints*.

Taylor, G. B., Carilli, C. L., and Perley, R. A. (1999). *Synthesis Imaging in Radio Astronomy II*. Astronomical Society of the Pacific, San Francisco, CA.

Tribble, P. C. (1991). Depolarization of extended radio sources by a foreground faraday screen. *Monthly Notices of the Royal Astronomical Society*, 250.

van Diepen, G. (2018). Dppp: Default pre-processing pipeline. `https://ui.adsabs.harvard.edu/abs/2018ascl.soft04003V/abstract`. Astrophysics Source Code Library.

van Weeren, R. J. (2019). Diffuse radio emission from galaxy clusters. *Space Science Reviews*.

van Weeren, R. J. (2021). Lofar observations of galaxy clusters in hetdex: Extraction and self-calibration of individual lofar targets. *Astronomy & Astrophysics*, 651.